Journal of Medicinal Chemistry

pubs.acs.org/jmc Article

3,4-Dihydropyrimidin-2(1*H*)-ones as Antagonists of the Human A_{2B} Adenosine Receptor: Optimization, Structure–Activity Relationship Studies, and Enantiospecific Recognition

María Majellaro,[¶] Willem Jespers,[¶] Abel Crespo,[¶] María J. Núñez, Silvia Novio, Jhonny Azuaje, Rubén Prieto-Díaz, Claudia Gioé, Belma Alispahic, José Brea,* María I. Loza, Manuel Freire-Garabal, Carlota Garcia-Santiago, Carlos Rodríguez-García, Xerardo García-Mera, Olga Caamaño, Christian Fernandez-Masaguer, Javier F. Sardina, Angela Stefanachi, Abdelaziz El Maatougui, Ana Mallo-Abreu, Johan Åqvist, Hugo Gutiérrez-de-Terán,* and Eddy Sotelo*

Cite This: *J. Med. Chem.* 2021, 64, 458–480 Read Online

ACCESS | Metrics & More | Article Recommendations | Supporting Information

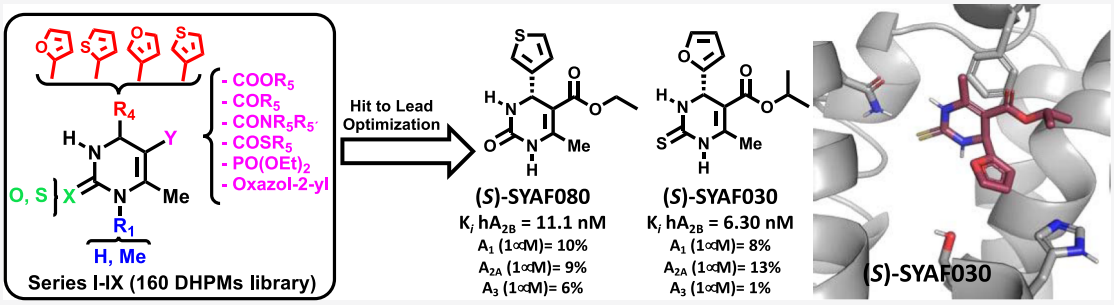

ABSTRACT: We present and thoroughly characterize a large collection of 3,4-dihydropyrimidin-2(1*H*)-ones as A_{2B}AR antagonists, an emerging strategy in cancer (immuno) therapy. Most compounds selectively bind A_{2B}AR, with a number of potent and selective antagonists further confirmed by functional cyclic adenosine monophosphate experiments. The series was analyzed with one of the most exhaustive free energy perturbation studies on a GPCR, obtaining an accurate model of the structure–activity relationship of this chemotype. The stereospecific binding modeled for this scaffold was confirmed by resolving the two most potent ligands [(±)-**47**, and (±)-**38** K_i = 10.20 and 23.6 nM, respectively] into their two enantiomers, isolating the affinity on the corresponding (*S*)-eutomers (K_i = 6.30 and 11.10 nM, respectively). The assessment of the effect in representative cytochromes (CYP3A4 and CYP2D6) demonstrated insignificant inhibitory activity, while in vitro experiments in three prostate cancer cells demonstrated that this pair of compounds exhibits a pronounced antimetastatic effect.

INTRODUCTION

Since its identification and cloning in the early 1990s, A_{2B} remains the most enigmatic of the four adenosine receptors (ARs).[1,2] Initially, this receptor was seen as a low-affinity (adenosine binds with an EC_{50} = 24 μM) version of the A_{2A}AR, with which it is often co-expressed in many tissues. These observations lead to the initial idea that the A_{2B}AR was a receptor with scarce physiological relevance,[3−5] which was later ruled out due to the characterization of distinctive intracellular signaling pathways, body distribution, and physiological roles between these two subtypes of ARs.[6−12] High levels of A_{2B}AR have been detected in neurons,[13] astrocytes,[14] and various immune cells,[15−18] and it has been confirmed that its expression is heavily affected by environmental cues such as inflammation, cell stress, injury, and hypoxia.[19−21] Accordingly, the A_{2B}AR is involved in diverse and relevant biological processes (e.g. vascular tone, cardiac myocyte contractility, penile erection, glucose homeostasis, pulmonary inflammation, inflammation, and pain).[22] Paradoxically, the reason for the initial low interest in A_{2B}AR (namely its low affinity for adenosine) potentially turns this receptor into an excellent therapeutic target for highly relevant related pathologies,[12,22] since it becomes activated under very specific pathological conditions (i.e. micromolar adenosine concentrations).

The relevance of the A_{2B}AR in cancer progression has been recognized recently, with increasing evidence demonstrating

Received: August 18, 2020
Published: December 29, 2020

https://dx.doi.org/10.1021/acs.jmedchem.0c01431
J. Med. Chem. 2021, 64, 458–480

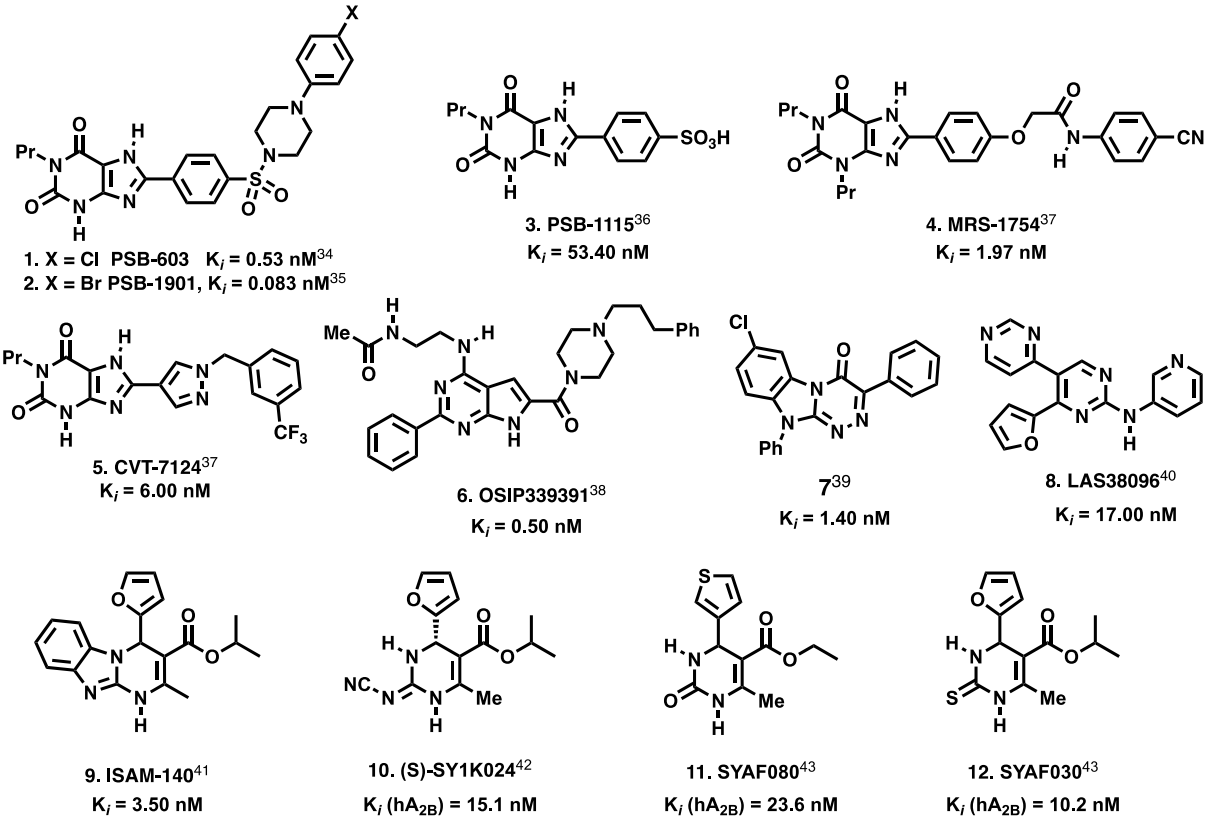

Figure 1. Structures of representative A_{2B}AR antagonists.[34−43]

its protumorigenic role in multiple types of cancer cells.[23−25] Growing evidence supports that the A_{2B}AR promotes tumor progression in many ways, eliciting key roles during tumor proliferation, angiogenesis, chemoresistance, metastasis, and immune suppression.[26−31] Consistent with this, high levels of A_{2B}AR are generally associated with worse prognosis in several cancer types.[25] Comparative analysis has shown that the A_{2B}AR is particularly highly expressed in human prostate cancer tissues as compared to prostatic healthy tissues.[32] Recent studies employing **PSB603**[32,33] (Figure 1, compound 1), a selective sub-nanomolar A_{2B}AR antagonist, documented its antitumor effect in PCa cells[32] and also the suppression of tumor growth and metastasis by inhibiting induction of regulatory T cells.[33] Moreover, data emerging from the study of the adenosine check point in cancer immunotherapy are progressively demonstrating highly relevant functions for the A_{2B}AR.[25,28,29] Accordingly, A_{2B}AR antagonists are emerging as promising anticancer agents that can take advantage of the central roles of adenosine in the tumor microenvironment.[25,28,29]

The elucidation of the functional roles and therapeutic potential of the A_{2B}AR has been partially hampered by the limited availability of potent and specific ligands and molecular probes.[44−48] While some compounds have reached clinical trials,[25,46] the chemical space explored by the current A_{2B}AR agonists is still limited,[44−48] and the best characterized A_{2B}AR antagonists are mainly xanthine congeners (Figure 1).[34−43] Hence, novel prototypic structures providing unexplored topologies, physicochemical features, and alternative binding modes are in demand.[46,47] In this scenario, we recently documented novel series of potent A_{2B}AR antagonists assembled by a Biginelli multicomponent approach (Figure 1, cpds **9**−**12**).[41−43] The chiral center in these chemotypes imposes critical topological features, differentiating themselves from classical A_{2B}AR ligands and modifying their biological profile from quantitative and qualitative points of view. Thus, in addition to its low nanomolar affinities and selectivity, their antagonistic effect is mediated by a previously unexplored stereospecific recognition at the A_{2B}AR.[42,43,49]

In this work, we report an exhaustive exploration of the structural determinants governing the A_{2B}AR antagonistic effect of the 3,4-dihydropyrimidin-2(1*H*)-one (DHPM) scaffold (Figure 1, cmpd **11**), discovered by our group together with the analogous series of 3,4-dihydropyrimidin-2(1*H*)-thiones (Figure 1, cmpd **12**).[48] A large library, consisting of 160 derivatives, was conceived to assess the contribution of the diverse positions in the heterocyclic core, with particular emphasis in the exploration of bioisosteric replacements for the ester function at position 5. The study also included the elucidation of the structure−activity relationship (SAR) and assessment of the initially proposed enantiospecific recognition at the A_{2B}AR by computational modeling using intensive free energy perturbation (FEP) calculations. The impact of the stereochemistry at position 4 in these series was confirmed by separation of the two most potent ligands (**38** and **47**) into their enantiomers, followed by pharmacological evaluation confirming the enantiospecific binding to the A_{2B}AR. Finally, a preliminary exploration of the antitumoral potential of ligands **38** and **47** demonstrated a potent antimigratory effect in three cellular models of PCa.

RESULTS AND DISCUSSION

Design. Our early report, documenting the original A_{2B}AR antagonistic effect of 34 DHPMs, included a preliminary

https://dx.doi.org/10.1021/acs.jmedchem.0c01431
J. Med. Chem. 2021, 64, 458−480

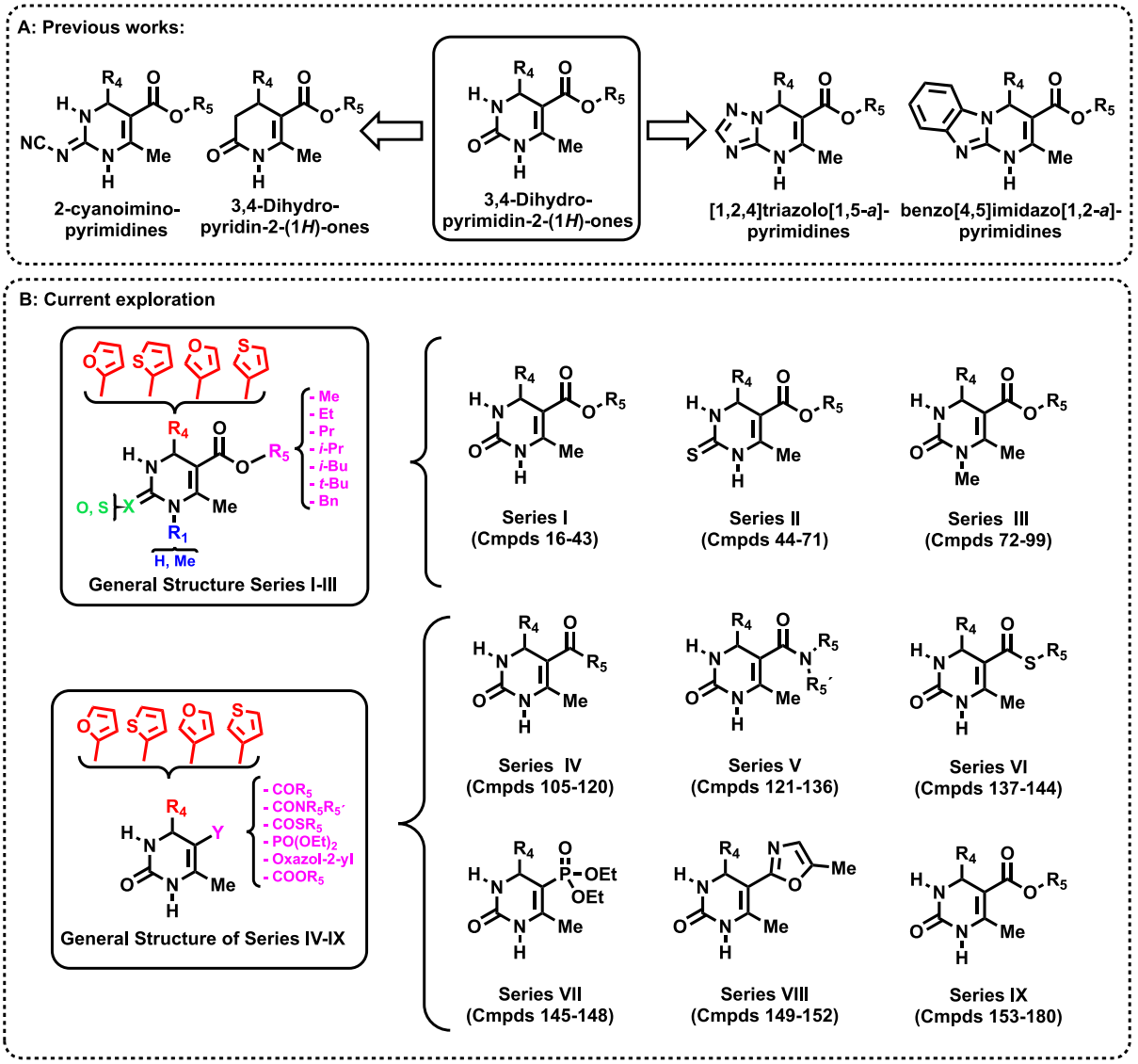

Figure 2. General structure of previously explored chemotypes (panel A) and novel series herein documented (panel B, series **I**–**IX**).

exploration of some SAR trends and the proposal of a binding mode for this scaffold.[43] In subsequent studies, we focused on the evaluation of different points of variability around the DHPM scaffold. The definition of the optimal substituents in R_4[50] was soon followed by scaffold hoping, investigating the effect of fusing other heterocycles at positions 2 and 3 of the pyrimidin-2-one core (Figure 2, panel A)[41] and the impact of bioisosteric replacements at either position 2 or 3 (Figure 2, panel A).[41,42] The SAR data accumulated in these studies was rationalized on the basis of the A_{2B}AR stereoselective binding mode originally proposed by us[43] and constituted the basis to guide the design of 136 new DHPMs, herein synthesized and characterized, which we have now divided into nine series (Figure 2, panel B). The integrated synthesis, binding data, SAR, and computational studies of the complete ligand library are described in this manuscript. Three initial subsets (Figure 2, panel B, series **I**–**III**) were conceived to complement the SAR exploration of our original report,[43] by modification of the substituents at positions 1, 2, 4, and 5 (Figure 2, panel B). The diversity of space explored was envisaged to assess distinctive structural features (e.g. electronic, steric, or lipo/hydrophilic) within the heterocyclic core (Figure 2). These include the replacement of 3,4-dihydropyrimidin-2(1*H*)-one/thione (series **I**/**II**, respectively, Figure 2 panel B) and the methylation of N_1 (series **III**). Since the introduction of aryl, alkyl, or cycloalkyl groups at R_4 produced inactive compounds,[50] we maintained the original set of pentagonal heteroaryl group (e.g. 2-furyl, 3-furyl and 2-thienyl, and 3-thienyl) characteristics of the ligands with highest A_{2B}AR affinity. For these three early subsets (**I**–**III**), seven alkyl residues (Me, Et, Pr, *i*-Pr, *i*-Bu, *t*-Bu, and Bn) were explored in the ester function (R_5). Series **IV**–**IX** (Figure 2 panel B) were designed to complete the evaluation of the influence of R_5 on the A_{2B}AR affinity and AR selectivity profiles. The design of each subset was conceived to analyze different bioisosteric replacements (subsets **IV**, **V**, **VI**, and **VII**). We then moved to evaluate the effect of cycle creation with series **VIII**. Finally, as the biological evaluation of series **IV**–**VIII** unequivocally identified an aliphatic ester as the optimum group in R_5, a new subset (**IX**) was designed to expand the diversity of the alkoxy group in the ester on this position (Figure 2, panel B).

Chemistry. The library, consisting of 160 AR ligands (cpds **16**–**99** and **105**–**180**), was assembled by following different experimental protocols based on the highly reliable Biginelli

https://dx.doi.org/10.1021/acs.jmedchem.0c01431
J. Med. Chem. 2021, 64, 458−480

Scheme 1. Synthesis of 3,4-Dihydropyrimidin-2-one/thione Series I–III (Cpds 16–99)

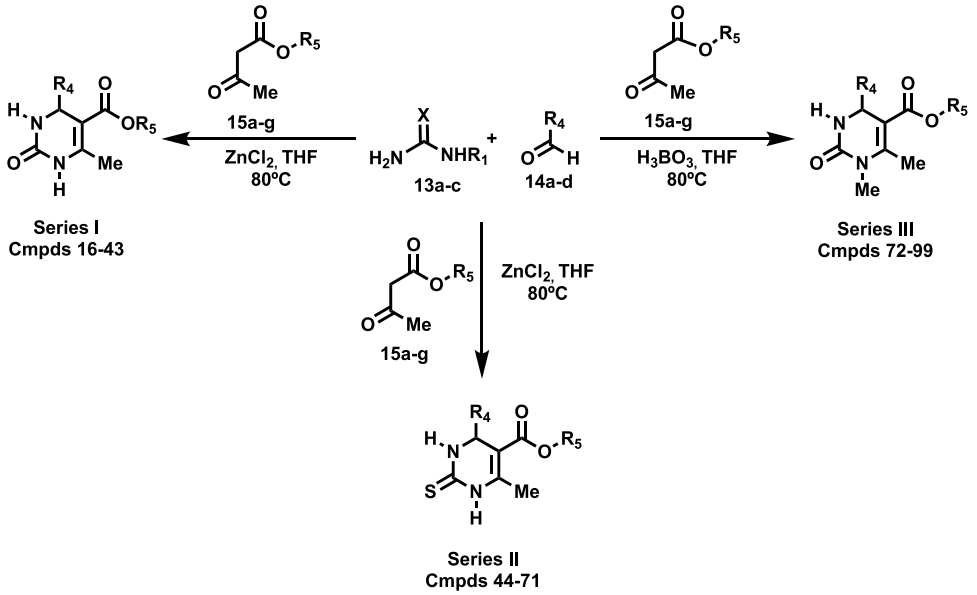

Scheme 2. Synthesis of 3,4-Dihydropyrimidin-2-one Series IV–VI (Cpds 105–144)

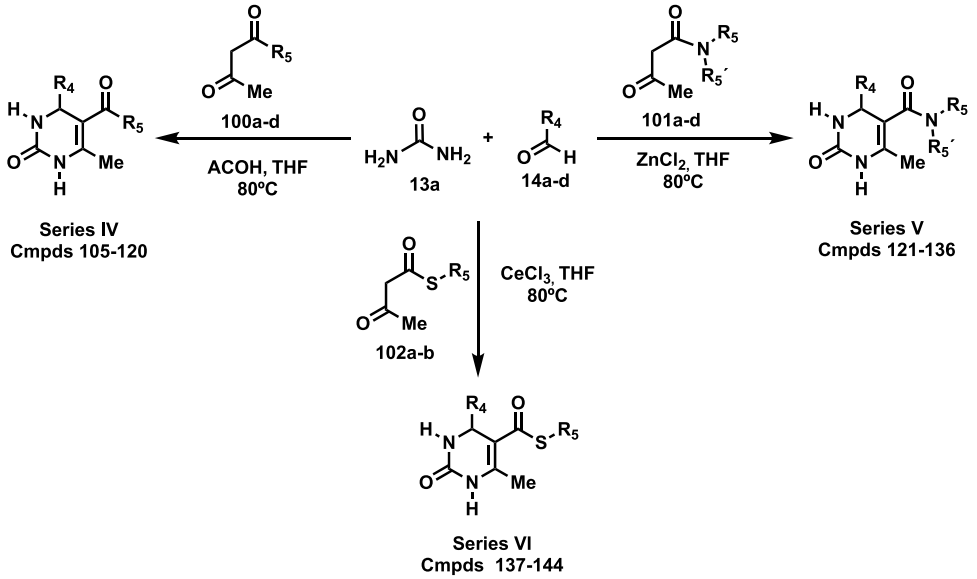

three-component reaction.[51,52] The experimental conditions of the synthetic pathways are depicted in Schemes 1–3. In a typical experiment, the urea derivative (**13a–c**) was combined with a pentagonal heterocyclic aldehyde (**14a–d**), a methylene-activated carbonyl compound [e.g. keto-esters (**15a–n**), diketones (**100a–d**), keto-amides (**101a–d**), keto-thioesters (**102a–b**), keto-phosphonate (**103**) or keto-1,3-oxazole (**104**)], and the appropriate catalyst. The reaction mixture was heated at 80 °C during variable reaction times (6–24 h). Due to the reactivity differences among the methylene-activated carbonyl compounds (**15**, **100**, **101**, **102**, **103**, and **104**) and being aware that the efficiency of the Biginelli reaction is dependent of the catalyst employed,[51,52] the optimal catalyst for each series was identified during preliminary experiments (Schemes 1–3). Targeted pyrimidine derivatives (**16–99** and **105–180**) were obtained in variable yields (37–90%) after appropriate purification (i.e. chromatographic methods or recrystallization).

The synthesized compounds were organized in nine subsets (Figure 2, panel B); the structures are depicted in Tables 1–8. Within the first three series (**I**, **II**, and **III**), 8 out of the 28 compounds within each subset correspond to previously reported compounds (denoted with an asterisk in Tables 1–3 and the corresponding references included in the Supporting Information). Series **IV–IX** contained 16, 16, 8, 4, 4, and 28 new ligands, respectively (Tables 4–8). As in previous studies,[41–43,49] all ligands were tested as racemic mixtures and this data constituted the basis to explore the SAR. Thereafter, the most appealing A_{2B}AR antagonists were separated into its enantiomers, their configuration was established by circular dichroism (CD), and then, its binding affinity at all four Ars was evaluated for each stereoisomer. A full account of the synthesis, structural, and characterization data for all compounds is provided in the Supporting Information.

https://dx.doi.org/10.1021/acs.jmedchem.0c01431
J. Med. Chem. 2021, 64, 458–480

Scheme 3. Synthesis of 3,4-Dihydropyrimidin-2-one Series VII–IX (Cpds 145–180)

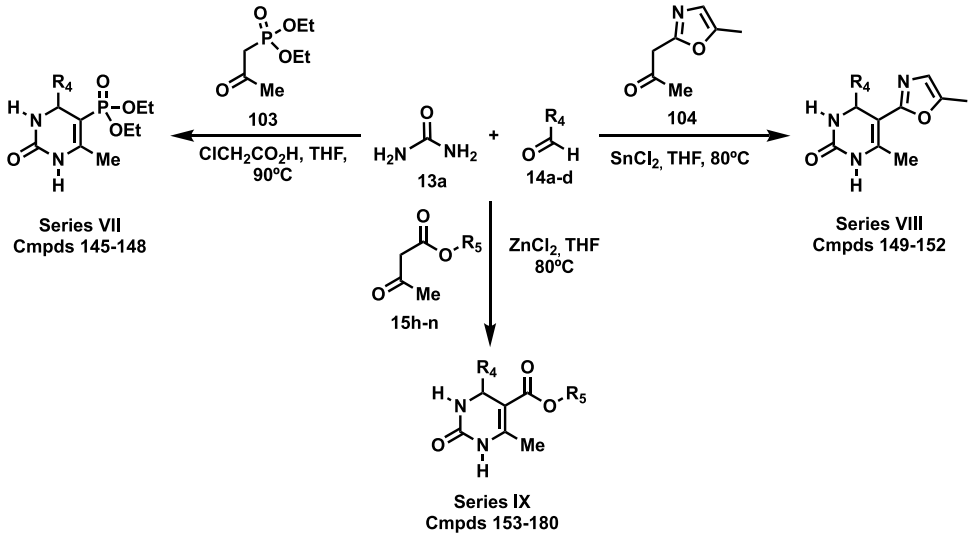

Biological Evaluation. The affinities for the four human AR (hAR) subtypes (A_1, A_{2A}, A_{2B}, and A_3) of the 160 3,4-dihydropyrimidin-2-one/thiones obtained (**16–99** and **105–180**) were evaluated in vitro (radioligand binding assays)[41–43,49] and reported in Tables 1–8. hARs expressed in transfected Chinese hamster ovary (CHO) (A_1AR), HeLa (A_{2A}AR and A_3AR), and HEK-293 (A_{2B}AR) cells were employed. [^{3}H]DPCPX for A_1AR and A_{2B}AR, [^{3}H]ZM241385 for A_{2A}AR, and [^{3}H]NECA for A_3AR were used as radiotracers during binding assays. The affinity data obtained for the racemic mixture of each compound is provided in Tables 1–8. The biological data are expressed as K_i ± standard error of the mean (SEM) (nM, n = 3) or as percentage inhibition of specific binding at 1 μM (n = 2, average) for those compounds that did not fully displace specific radioligand binding. K_i values were obtained by fitting the data with nonlinear regression using Prism 2.1 software (GraphPad, San Diego, CA). The binding affinity obtained for representative AR antagonists (**ISAM-140**, **ZM241385**, and **DPCPX**), using the binding protocols herein employed, was included in Tables 1–8 for comparative purposes.

Functional Experiments. *Cyclic Adenosine Monophosphate Assays.* The two most potent compounds of the series (**38** and **47**) were evaluated in cyclic adenosine monophosphate (cAMP) assays to determinate their ability to inhibit NECA-stimulated (100 nM) cAMP production.[41–43,49] The log concentration–response curves of c-AMP accumulation for selected antagonists to hA_{2B}ARs are presented in Figure 3. These experiments demonstrated that compounds **38** and **47** inhibit NECA-induced c-AMP accumulation, unequivocally validating their antagonism at hA_{2B}ARs. Analysis of the K_i and K_B values shows low nanomolar range data obtained during binding (K_i = 23.6 and 10.2 nM, respectively) and functional experiments (K_B = 25.2 and 4.7 nM, respectively).

Enantiospecific Binding to the A_{2B}AR. As indicated above, all compounds here reported were obtained and tested as racemates (Tables 1–8). However, both our initial molecular models[48] and results from the FEP calculations (see previous section) indicate that only one enantiomer should bind the orthosteric site of the receptor. The importance of the stereogenic center at the heterocyclic core during the recognition at the A_{2B}AR binding pocket was also inferred during our early SAR exploration of the DHPM scaffold.[43] It was observed that aromatization of the 3,4-dihydropyrimidin-2(1*H*)-one/thione nucleus abolished the A_{2B}AR affinity for ligands **38** and **47**.[43] In addition, in our recent studies with other structurally related scaffolds,[42,43] the most attractive ligands were separated and the corresponding active stereoisomer correlated with these predictions. Following this line of reasoning, we proceeded to the enantiomeric separation and assignment of the most attractive compounds within series **I–IX** [(±)-**38** and (±)-**47**], followed by their biological evaluation.

Figure 4 shows the results of our joint approach using chiral high-performance liquid chromatography (HPLC) and CD spectroscopy. As recently documented by our own results with structurally related Biginelli-like systems[42,49] as well as for other pharmacologically active 3,4-dihydropyrimidin-2-ones/thiones,[61–63] the sign of the distinctive CD activity of the enamide group (around 300 nm) allows the unequivocal assignment of the absolute configuration of each enantiomer (Figure 4). Semipreparative HPLC separation of the selected racemic ligands [(±)-**38** and (±)-**47**] on a chiral stationary phase (Figure 4 and Experimental Section) afforded each enantiomer with excellent stereochemical purity (97 and 99% respectively). At this wavelength, enantiomers showing a negative Cotton effect (red line) contain the pentagonal heterocycle (furan or thiophene) backward [which corresponds to (4*S*)-**38** and (4*S*)-**47**, respectively] while the stereoisomers giving a positive Cotton effect (blue line) contain the heterocyclic core forward [which corresponds to (4*R*)-**38** and (4R)-**47**, respectively].

The biological profiles of the isolated enantiomers [(*R*)-**38**, (*S*)-**38**, (*R*)-**47**, and (*S*)-**47**] were then evaluated at the four hARs, and the resulting data (Table 9) are compared to the corresponding racemic mixtures [(±)-**38** and (±)-**47**]. With this analysis, we could confirm that the A_{2B}AR affinity exhibited by the racemic mixture of **38** and **47** is exclusively due to the (*S*)-**38** and (*S*)-**47** enantiomers (K_i = 11.1 and 6.30 nM). In both cases, the eutomer [the (*S*) stereoisomer] is nearly twofold more potent than the racemic mixture [**38**, (K_i = 23.6 nM), **47**, (K_i = 10.2 nM)], whereas (*R*)-stereoisomers are devoid of any affinity at the four ARs (Table 9). To

https://dx.doi.org/10.1021/acs.jmedchem.0c01431
J. Med. Chem. 2021, 64, 458–480

Table 1. Structure and Binding Data for the 3,4-Dihydropyridin-2(1*H*)-ones 16−43 at the hARs (Subset I, Figure 2)

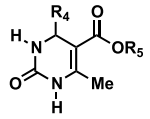

			K_i (nM) or % at 1 μM[a]			
compound	R_4	R_5	hA_1[b]	hA_{2A}[c]	hA_{2B}[d]	hA_3[e]
16[43]	2-furyl	Me	34%	25%	2159 ± 232	13%
17[43]	2-furyl	Et	15%	31%	585 ± 89	2%
18[43]	2-furyl	*n*-Pr	43%	55%	206 ± 11	3%
19[43] (**SYAF014**)	2-furyl	*i*-Pr	18%	23%	40.8 ± 2.3	4%
20	2-furyl	*i*-Bu	27%	36%	199 ± 11	13%
21	2-furyl	*t*-Bu	4%	7%	44%	7%
22	2-furyl	Bn	36%	26%	887 ± 30	3%
23	3-furyl	Me	8%	3%	42%	2%
24[43] (**SYAF101**)	3-furyl	Et	21%	24%	39.6 ± 1.1	1%
25	3-furyl	*n*-Pr	50%	45%	1192 ± 107	11%
26[43]	3-furyl	*i*-Pr	25%	26%	1486 ± 62	3%
27	3-furyl	*i*-Bu	3088 ± 88	31%	326 ± 7	16%
28[53]	3-furyl	*t*-Bu	11%	9%	4436 ± 182	2%
29	3-furyl	Bn	41%	24%	6650 ± 210	1%
30[54]	2-thienyl	Me	6%	1%	19%	3%
31[43]	2-thienyl	Et	1%	33%	41%	1%
32	2-thienyl	*n*-Pr	43%	30%	1519 ± 117	32%
33[43]	2-thienyl	*i*-Pr	37%	19%	44%	14%
34	2-thienyl	*i*-Bu	25%	12%	2130 ± 88	11%
35[55]	2-thienyl	*t*-Bu	26%	10%	38%	7%
36[56]	2-thienyl	Bn	45%	30%	1916 ± 110	8%
37[57]	3-thienyl	Me	7%	2%	36%	3%
38[43] (**SYAF080**)	3-thienyl	Et	16%	34%	23.6 ± 1.0	11%
39	3-thienyl	*n*-Pr	44%	48%	201 ± 3	6%
40[43] (**SYAF020**)	3-thienyl	*i*-Pr	26%	25%	56.6 ± 1.3	5%
41	3-thienyl	*i*-Bu	56%	37%	1188 ± 110	21%
42[55]	3-thienyl	*t*-Bu	15%	5%	47%	1%
43	3-thienyl	Bn	57%	21%	44%	25%
ISAM-140			20%	25%	3.49 ± 0.2	2%
ZM241385			683 ± 4	1.9 ± 0.1	65.7 ± 1.7	863 ± 4
DPCPX			2.20 ± 0.2	157 ± 2.9	73.24 ± 2.0	1722 ± 11

[a] $n = 3$ for K_i values, or $n = 2$ for percentage displacement of specific binding. [b] Displacement of specific [^{3}H]DPCPX binding in adenosine A_1 receptors expressed in human CHO cells. [c] Displacement of specific [3]ZM2421385 binding in adenosine A_{2A} receptors expressed in human HeLa cells. [d] Displacement of specific [^{3}H]DPCPX binding in human HEK-293 cells. [e] Displacement of specific [^{3}H]NECA binding in adenosine A_3 receptors expressed in human HeLa cells.

provide a further structural rationale, we calculated the energetic difference between both enantiomers of compound **47** via direct FEP simulations between the compound pair, starting from the binding model proposed in each case (see Figure S4). The simulations agree with the experimental data, indicating stark binding preference for the most potent eutomer ($\Delta\Delta G$ = 6.04 ± 1.06 kcal/mol). These data constitute a remarkable example of A_{2B}AR antagonists that exhibit enantiospecific recognition profiles, which is satisfactorily explained with the binding mode hypothesis behind the design of this series, in agreement with our observations for structurally related Biginelli-based scaffolds.[50]

SAR Analysis and Molecular Modeling. The biological evaluation of the nine series of DHPMs (Tables 1−8) allowed us to identify eight potent (K_i < 100 nM) and specific A_{2B}AR ligands, for example, compounds **19**, **24**, **38**, and **40** (Table 1), **47** and **52** (Table 2), and **154** and **155** (Table 8). Additionally, a dozen of DHPMs exhibited moderate (K_i 100−500 nM) A_{2B}AR affinity (e.g. compounds **18**, **20**, **27**, **39**, **54**, **68**, **108**, **158**, **161**, **162**, **165**, and **176**), while still retaining the excellent selectivity profile characteristic of these series. The most interesting DHPMs contained an exocyclic carbonyl group at position 2 and no substituent at positions 1 and 3 (series **I**, **IV**−**IX**), while the most potent A_{2B}AR antagonist (**47**, K_i = 10.2 nM) belongs to the bioisosteric 3,4-dihydropyrimidin-2(1*H*)-thione series **II** (Table 2). The first part of the SAR analysis is focused on the first three subsets (Figure 2, series **I**−**III**), exploring precisely the effect of the O/S bioisosteric replacement at position 2 of the DHPM scaffold (series II) as well as methylation on N_1 (series **III**). All these series maintain a substituted ester group (position 5), and the impact of bioisosteric replacement of this functionality is further analyzed in subsets **IV**−**VIII**. It will be deduced that collectively, the most appealing A_{2B}AR affinities within series **I**−**VIII** are indeed within the first subset of DHPMs (Table 1, compounds **16**−**43**). This motivated an expansion of the diversity of the alkyl residues at the ester group (subset **IX**), which will be analyzed in depth through

https://dx.doi.org/10.1021/acs.jmedchem.0c01431
J. Med. Chem. 2021, 64, 458−480

Table 2. Structure and Binding Data for the 3,4-Dihydropyridin-2(1*H*)-thiones 44−71 at the hARs (Subset II, Figure 2)

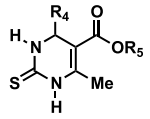

			K_i (nM) or % at 1 μM[a]			
compound	R_4	R_5	hA_1[b]	hA_{2A}[c]	hA_{2B}[d]	hA_3[e]
44[54]	2-furyl	Me	11%	20%	984 ± 52	1%
45[43]	2-furyl	Et	1%	32%	608 ± 31	5%
46	2-furyl	*n*-Pr	1%	2%	46%	1%
47[43] (**SYAF030**)	2-furyl	*i*-Pr	15%	18%	10.2 ± 0.5	1%
48	2-furyl	*i*-Bu	7%	30%	18%	10%
49	2-furyl	*t*-Bu	3%	1%	9%	9%
50	2-furyl	Bn	32%	12%	41%	4%
51	3-furyl	Me	25%	1%	48%	3%
52[43]	3-furyl	Et	18%	25%	43.1 ± 1.6	15%
53	3-furyl	*n*-Pr	4%	2%	45%	3%
54[43]	3-furyl	*i*-Pr	18%	33%	194 ± 12	23%
55	3-furyl	*i*-Bu	12%	35%	1%	1%
56	3-furyl	*t*-Bu	18%	15%	1893 ± 88	19%
57	3-furyl	Bn	25%	16%	36%	20%
58	2-thienyl	Me	1%	1%	10%	1%
59[43]	2-thienyl	Et	2%	23%	3247 ± 101	4%
60[58]	2-thienyl	*n*-Pr	7%	1%	3%	10%
61[43]	2-thienyl	*i*-Pr	23%	15%	1572 ± 93	20%
62[58]	2-thienyl	*i*-Bu	1%	2%	12%	4%
63	2-thienyl	*t*-Bu	22%	7%	26%	22%
64[58]	2-thienyl	Bn	34%	63%	45%	24%
65	3-thienyl	Me	3%	1%	38%	3%
66[43]	3-thienyl	Et	23%	28%	1103 ± 94	2%
67	3-thienyl	*n*-Pr	5%	1%	26%	1%
68[43]	3-thienyl	*i*-Pr	16%	20%	315 ± 7	3%
69	3-thienyl	*i*-Bu	8%	1%	15%	2%
70	3-thienyl	*t*-Bu	16%	22%	26%	16%
71	3-thienyl	Bn	3%	16%	10%	2%
ISAM-140			20%	25%	3.49 ± 0.2	2%
ZM241385			683 ± 4	1.9 ± 0.1	65.7 ± 1.7	863 ± 4
DPCPX			2.20 ± 0.2	157 ± 2.9	73.24 ± 2.0	1722 ± 11

[a] n = 3 for K_i values, or n = 2 for percentage displacement of specific binding. [b] Displacement of specific [^{3}H]DPCPX binding in adenosine A_1 receptors expressed in human CHO cells. [c] Displacement of specific [3]ZM2421385 binding in adenosine A_{2A} receptors expressed in human HeLa cells. [d] Displacement of specific [^{3}H]DPCPX binding in human HEK-293 cells. [e] Displacement of specific [^{3}H]NECA binding in adenosine A_3 receptors expressed in human HeLa cells.

the last section of this SAR study. The effect of all these structural modifications on binding affinity will be systematically assessed by FEP calculations, performed on the basis of the binding mode previously proposed and here refined for the A_{2B}AR.[49]

The first general SAR observation is the systematic drop in affinity to negligible values due to methylation on position N_1 of the pyrimidine scaffold observed along subset **III** (Table 3, **72**−**99**). Notably, this effect is not compensated by any substituents explored at either R_4 or R_5. Within the first subsets, the effect of the pentagonal heterocycle at position 4 also shows some clear tendencies: 2-furyl-, 3-furyl-, and 3-thienyl-substituted ligands exert higher affinities as compared to the 2-thienyl substituted ligands. This is clearly exemplified in Figure 5, showing a comparison of the most active compound within each series (**I**−**III**). In this case, however, the effect is variable depending on the substituent at R_5. In general, the exploration of the R_5 chain on the ester group reveals a size dependency, that is, from the smallest to the largest substitution (Me to Bn), with optimal affinities observed for medium sized substituents (Et, *i*-Pr).

The observed SAR trends generally support the binding orientation previously proposed for this chemotype, here illustrated in Figure 5 for the DHPM scaffold after further refinement (see below).[43] This model resulted from a docking exploration of compound **38** (subset **I**) using a homology model of the hA_{2B}AR based on the X-ray structure of the A_{2A}AR[65] and retained two key interactions conserved in most AR antagonists: a hydrogen bond with the AR-conserved residue N254$^{6.55}$, achieved via the oxygen atom at position 2 of the ligand, and the $\pi-\pi$ stacking of the core ring with F173^{EL2}. These interactions are complemented by an enantiospecific shape complementarity between the L-shape formed by the pyrimidinone core and the ring at R_4 and the A_{2B}AR specific residue V250$^{6.51}$, providing a possible source of selectivity versus other AR members (containing a bigger Leu).[43] A similar binding orientation was found for the structural analogues bicyclic and tricyclic scaffolds,[41] including

https://dx.doi.org/10.1021/acs.jmedchem.0c01431
J. Med. Chem. 2021, 64, 458−480

Table 3. Structure and Binding Data for the 3,4-Dihydropyridin-2(1*H*)-ones 72−99 at the hARs (Subset III, Figure 2)

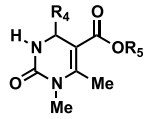

			K_i (nM) or % at 1 μM[a]			
compound	R_4	R_5	hA_1[b]	hA_{2A}[c]	hA_{2B}[d]	hA_3[e]
72	2-furyl	Me	45%	1%	31%	9%
73[43]	2-furyl	Et	17%	1%	6544 ± 101	25%
74	2-furyl	*n*-Pr	3%	2%	23%	8%
75[43]	2-furyl	*i*-Pr	29%	37%	1151 ± 23	18%
76	2-furyl	*i*-Bu	13%	3%	4%	23%
77	2-furyl	*t*-Bu	44%	20%	26%	54%
78	2-furyl	Bn	1736 ± 89	37%	41%	11%
79	3-furyl	Me	15%	5%	7%	7%
80[43]	3-furyl	Et	17%	24%	4259 ± 95	1%
81	3-furyl	*n*-Pr	1%	1%	2%	16%
82[43]	3-furyl	*i*-Pr	23%	2%	37%	1%
83	3-furyl	*i*-Bu	4%	4%	1%	16%
84	3-furyl	*t*-Bu	21%	16%	16%	12%
85	3-furyl	Bn	51%	37%	49%	25%
86[59]	2-thienyl	Me	30%	49%	17%	15%
87[43]	2-thienyl	Et	1%	1%	11%	2%
88	2-thienyl	*n*-Pr	9%	1%	1%	4%
89[43]	2-thienyl	*i*-Pr	22%	24%	28%	17%
90	2-thienyl	*i*-Bu	9%	1%	2%	5%
91	2-thienyl	*t*-Bu	18%	12%	24%	22%
92	2-thienyl	Bn	50%	3%	50%	18%
93	3-thienyl	Me	24%	13%	26%	22%
94[43]	3-thienyl	Et	32%	23%	53%	3%
95	3-thienyl	*n*-Pr	2%	3%	1%	11%
96[43]	3-thienyl	*i*-Pr	35%	22%	51%	14%
97	3-thienyl	*i*-Bu	8%	2%	1%	4%
98	3-thienyl	*t*-Bu	18%	1%	35%	14%
99	3-thienyl	Bn	46%	30%	4521 ± 79	14%
ISAM-140			20%	25%	3.49 ± 0.2	2%
ZM241385			683 ± 4	1.9 ± 0.1	65.7 ± 1.7	863 ± 4
DPCPX			2.20 ± 0.2	157 ± 2.9	73.24 ± 2.0	1722 ± 11

[a]n = 3 for K_i values, or n = 2 for percentage displacement of specific binding. [b]Displacement of specific [^{3}H]DPCPX binding in adenosine A_1 receptors expressed in human CHO cells. [c]Displacement of specific [3]ZM2421385 binding in adenosine A_{2A} receptors expressed in human HeLa cells. [d]Displacement of specific [^{3}H]DPCPX binding in human HEK-293 cells. [e]Displacement of specific [^{3}H]NECA binding in adenosine A_3 receptors expressed in human HeLa cells.

a related series consisting of trifluorinated pyrimidine-based A_{2B}AR antagonists[49] as well as for the monocyclic cyanoimino derivatives.[42] In the last two cases, the stereospecific recognition hypothesized with molecular modeling was experimentally confirmed by enantiomeric separation of the most potent compounds by chiral HPLC followed by structural characterization by CD and X-ray determination of the most potent compounds.[42,49] It thus seemed reasonable to retain the equivalent active stereoisomer for modeling purposes of the current series, something that we would later evaluate by a similar experimental separation and evaluation of the stereoisomers of the most potent compounds here identified (see below). The binding orientation described for **38**[43] was used to create an analogous complex with the prototype compound **19**, which was here subject to a molecular dynamics (MD) equilibration. The resulting refined binding model importantly considers the role of water-mediated interactions and led to a slight shift of the position of the ligand, allowing for a second hydrogen bond between N254$^{6.55}$ and the NH at position 1 (see Figure 5), in analogy to the dual hydrogen bond observed between this residue and most co-crystallized AR ligands. This refined position was then used for a first series of FEP simulations, designed to evaluate if the proposed binding model could successfully explain the pronounced detrimental effect on methylation at N_1 (comparison between subsets **I** and **III**, Figure 5) as well as the role of the carbonyl/thiocarbonyl bioisosteric substitution at position 2, (i.e., comparison between equivalent ligand pairs of subsets **I** and **II**, see Figure 6). The FEP calculations covered all compound pairs between the two series to be compared, where at least one of the molecules involved showed measurable A_{2B} binding affinities (K_i < 1 μM), thus yielding 10 and 12 pair comparisons for subsets **I** → **III** and **I** → **II**.

The calculations of binding affinity differences between subsets **I** and **III** yielded excellent agreement with the experimental results (Figure 6, compare gray and blue bars) with a mean absolute error (MAE) of 0.71 kcal/mol over the

https://dx.doi.org/10.1021/acs.jmedchem.0c01431
J. Med. Chem. 2021, 64, 458−480

Table 4. Structure and Binding Data for the 3,4-Dihydropyridin-2(1*H*)-ones 105−120 at the hARs (Subset IV, Figure 2)

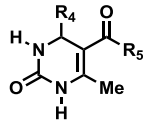

			K_i (nM) or % at 1 μM[a]			
compound	R_4	R_5	hA_1[b]	hA_{2A}[c]	hA_{2B}[d]	hA_3[e]
105[60]	2-furyl	Me	30%	21%	38%	14%
106	2-furyl	*c*-Pr	2%	2%	1062 ± 29	7%
107	2-furyl	*n*-Pr	1%	6%	807 ± 12	1%
108	2-furyl	*i*-Bu	16%	6%	240 ± 5	31%
109	3-furyl	Me	6%	1%	15%	2%
110	3-furyl	*c*-Pr	1%	1%	10%	16%
111	3-furyl	*n*-Pr	1%	2%	22%	2%
112	3-furyl	*i*-Bu	23%	20%	1008 ± 25	18%
113[60]	2-thienyl	Me	11%	2%	2%	3%
114	2-thienyl	*c*-Pr	1%	1%	1%	15%
115	2-thienyl	*n*-Pr	2%	23%	9%	2%
116	2-thienyl	*i*-Bu	19%	1%	43%	18%
117[60]	3-thienyl	Me	9%	1%	24%	1%
118	3-thienyl	*c*-Pr	2%	4%	1%	1%
119	3-thienyl	*n*-Pr	6%	11%	9%	1%
120	3-thienyl	*i*-Bu	37%	19%	1002 ± 11	14%
ISAM-140			20%	25%	3.49 ± 0.2	2%
ZM241385			683 ± 4	1.9 ± 0.1	65.7 ± 1.7	863 ± 4
DPCPX			2.20 ± 0.2	157 ± 2.9	73.24 ± 2.0	1722 ± 11

[a] $n = 3$ for K_i values, or $n = 2$ for percentage displacement of specific binding. [b] Displacement of specific [^{3}H]DPCPX binding in adenosine A_1 receptors expressed in human CHO cells. [c] Displacement of specific [3]ZM2421385 binding in adenosine A_{2A} receptors expressed in human HeLa cells. [d] Displacement of specific [^{3}H]DPCPX binding in human HEK-293 cells. [e] Displacement of specific [^{3}H]NECA binding in adenosine A_3 receptors expressed in human HeLa cells.

10 pair comparisons. According to the binding mode proposed (Figure 5A), the reason for the systematic reduction in affinity observed upon N_1-methylation can be found in the destabilization of the hydrogen bond with conserved N254$^{6.55}$. However, given the relative symmetry of the 3,4-dihydropyrimidinone scaffold, one cannot rule out the possibility of an alternate binding mode adopted by the methylated DHPM scaffold. This would meanwhile place the substituent at R_5 in the same extracellular binding crevice, as previously explored,[42,43] while satisfying the double hydrogen bond with N254$^{6.55}$ as illustrated in Figure 6B. To further analyze this possibility, we performed the corresponding FEP transformations using the alternative binding mode. The results, depicted in Figure 6C in orange bars, systematically predicted incorrect increases in binding affinity for the methylated compounds in subset **III**, in stark contrast with the experimental results (MAE = 3.59 kcal/mol). Thus, the simulations clearly support the stereospecific binding mode previously proposed[43] and here refined (Figure 6A). Consequently, we retained this binding mode as the starting point to explore the differences in affinity due to the thiocarbonyl substitution in position 2 (subset **II**). This single heteroatom substitution has a more spurious effect along the two subsets to be compared (**I** and **II**), as illustrated by a 4-fold increase in binding affinity observed between **19** and **47**, while the best compound in series **I** (**38**) dramatically loses affinity (50 fold) when transformed into the corresponding thienyl derivative **66**. On average, for the 12 compound pairs considered, the experimental effect of this bioisosteric substitution is milder than in the previous case of N_1 methylation ($\Delta\Delta G_{avg,exp}$ = 0.94 ± 1.35 kcal/mol). According to our binding model, the replacement of an oxygen by a bigger sulfur atom at position 2 produces a slight shift in the position of the ligand, which can lead to suboptimal accommodation of the remaining substituents, depending on the nature of R_4 and R_5. Encouragingly, this trend is also correctly reproduced by our theoretical calculations, and in most cases, the stabilizing or destabilizing effect of the bioisosteric replacement is correctly predicted (Figure 7, $\Delta\Delta G_{avg,calc}$ = 0.68 ± 0.87 kcal/mol, MAE = 1.17 kcal/mol).

The next cycle of FEP simulations was conceived to explore the effects of the different substitutions at R_5 (subsets **IV**−**IX**) on the A_{2B}AR affinity. This substituent would sit on a narrow region between TM2 and TM3 in the extracellular side of the binding cavity (Figure 7). The ester (subsets **I**−**III** and **IX**) or bioisosteric analogues (series **IV**−**VIII**) would displace the water molecules that eventually fill this region, which were initially occupying this pocket by analogy with the high-resolution crystal structure of the A_{2A}AR.[66] In this way, the alkyl chain on the functionalized ester (or by analogy on most of the bioisosteres), would sit in a relatively small and hydrophobic cavity defined by residues Ala64$^{2.61}$, Ile67$^{2.64}$, Ala82$^{3.29}$, and Val85$^{3.32}$. Indeed, on the basis of this binding mode, we could recently explain the succinct effect of fluorination in the functionalized ester substituents at R_5.[49] The limited size of this pocket also correlates with the SAR observation that larger hydrophilic changes result in loss of binding (in particular series **VII**). To assess these qualitative observations, we performed FEP calculations transforming R_5 between three reference compounds in series **I**, namely **19** (R_4 = 2-furyl, R_5 = CO_2−*i*-Pr, K_i = 40.8 nM), **24** (R_4 = 3-furyl, R_5 = CO_2−Et, K_i = 39.6 nM), and **38** (R_4 = 3-thienyl, R_5 =

https://dx.doi.org/10.1021/acs.jmedchem.0c01431
J. Med. Chem. 2021, 64, 458−480

Table 5. Structure and Binding Data for the 3,4-Dihydropyridin-2(1*H*)-ones 121−136 at the hARs (Subset V, Figure 2)

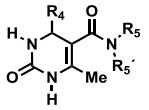

			K_i (nM) or % at 1 μM[a]			
compound	R_4	R_5, $R_{5'}$	hA_1[b]	hA_{2A}[c]	hA_{2B}[d]	hA_3[e]
121[43]	2-furyl	H, H	2%	1%	2%	2%
122	2-furyl	H, Et	2%	1%	1%	3%
123	2-furyl	H, *i*-Pr	3%	1%	2%	4%
124	2-furyl	Et, Et	11%	9%	31%	19%
125	3-furyl	H, H	1%	3%	6%	2%
126	3-furyl	H, Et	1%	2%	2%	1%
127	3-furyl	H, *i*-Pr	1%	1%	3%	3%
128	3-furyl	Et, Et	15%	6%	12%	37%
129	2-thienyl	H, H	2%	1%	3%	1%
130	2-thienyl	H, Et	1%	1%	1%	4%
131	2-thienyl	H, *i*-Pr	2%	22%	40%	1%
132	2-thienyl	Et, Et	13%	15%	22%	31%
133	3-thienyl	H, H	2%	18%	1%	1%
134	3-thienyl	H, Et	3%	17%	1%	1%
135	3-thienyl	H, *i*-Pr	8%	1%	3%	1%
136	3-thienyl	Et, Et	11%	9%	11%	35%
ISAM-140			20%	25%	3.49 ± 0.2	2%
ZM241385			683 ± 4	1.9 ± 0.1	65.7 ± 1.7	863 ± 4
DPCPX			2.20 ± 0.2	157 ± 2.9	73.24 ± 2.0	1722 ± 11

[a] n = 3 for K_i values, or n = 2 for percentage displacement of specific binding. [b] Displacement of specific [^{3}H]DPCPX binding in adenosine A_1 receptors expressed in human CHO cells. [c] Displacement of specific [3]ZM2421385 binding in adenosine A_{2A} receptors expressed in human HeLa cells. [d] Displacement of specific [^{3}H]DPCPX binding in human HEK-293 cells. [e] Displacement of specific [^{3}H]NECA binding in adenosine A_3 receptors expressed in human HeLa cells.

Table 6. Structure and Binding Data for the 3,4-Dihydropyridin-2(1*H*)-ones 137−144 at the hARs (Subset VI, Figure 2)

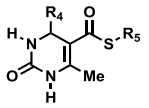

			K_i (nM) or % at 1 μM[a]			
compound	R_4	R_5	hA_1[b]	hA_{2A}[c]	hA_{2B}[d]	hA_3[e]
137	2-furyl	Et	6%	2%	29%	14%
138	2-furyl	*i*-Pr	5%	2%	22%	1%
139	3-furyl	Et	3%	1%	1%	1%
140	3-furyl	*i*-Pr	9%	2%	637 ± 28	3%
141	2-thienyl	Et	6%	8%	1%	1%
142	2-thienyl	*i*-Pr	1%	1%	1%	1%
143	3-thienyl	Et	11%	1%	17%	2%
144	3-thienyl	*i*-Pr	24%	2%	14%	1%
ISAM-140			20%	25%	3.49 ± 0.2	2%
ZM241385			683 ± 4	1.9 ± 0.1	65.7 ± 1.7	863 ± 4
DPCPX			2.20 ± 0.2	157 ± 2.9	73.24 ± 2.0	1722 ± 11

[a] n = 3 for K_i values, or n = 2 for percentage displacement of specific binding. [b] Displacement of specific [^{3}H]DPCPX binding in adenosine A_1 receptors expressed in human CHO cells. [c] Displacement of specific [3]ZM2421385 binding in adenosine A_{2A} receptors expressed in human HeLa cells. [d] Displacement of specific [^{3}H]DPCPX binding in human HEK-293 cells. [e] Displacement of specific [^{3}H]NECA binding in adenosine A_3 receptors expressed in human HeLa cells.

CO_2−Et, K_i = 23.6 nM) and their counterparts in series **IV**−**IX**. In other words, each parent compound in series **I** was compared to an array of 19 compounds which differ on R_5, while maintaining the corresponding R_4 substituent in each case (see Tables S1−S3 in the Supporting Information). The replacement of the ester function to different bioisosteres, namely ketone (subset **IV**), amide (subset **V**), thioamide (subset **VI**), phosphate (series **VII**), or oxazolyl (subset **VIII**) functions, results in all cases in a moderate to complete loss of experimental affinity (Tables 4−7), which is correctly modeled by the corresponding FEP transformations in all cases (Tables S1−S3). The mildest reduction in affinity is observed in subset **IV**, where a ketone in R_5 in combination with 2-furyl in R_4 (Table 4, compounds **105**−**108**) yields

https://dx.doi.org/10.1021/acs.jmedchem.0c01431
J. Med. Chem. 2021, 64, 458−480

Table 7. Structure and Binding Data for the 3,4-Dihydropyridin-2(1*H*)-ones 145−152 at the hARs (Series VII and VIII, Figure 2)

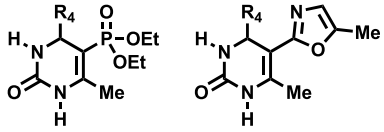

Series VII (Cmpds 145-148) Series VIII (Cmpds 149-152)

		K_i (nM) or % at 1 μM[a]			
compound	R_4	hA_1[b]	hA_{2A}[c]	hA_{2B}[d]	hA_3[e]
145	2-furyl	3%	4%	2%	4%
146	3-furyl	1%	8%	3%	2%
147	2-thienyl	2%	5%	7%	5%
148	3-thienyl	4%	3%	1%	1%
149	2-furyl	27%	23%	905 ± 39	4%
150	3-furyl	21%	14%	801 ± 13	1%
151	2-thienyl	21%	7%	45%	1%
152	3-thienyl	34%	20%	1126 ± 45	2%
ISAM-140		20%	25%	3.49 ± 0.2	2%
ZM241385		683 ± 4	1.9 ± 0.1	65.7 ± 1.7	863 ± 4
DPCPX		2.20 ± 0.2	157 ± 2.9	73.24 ± 2.0	1722 ± 11

[a] n = 3 for K_i values, or n = 2 for percentage displacement of specific binding. [b] Displacement of specific [^{3}H]DPCPX binding in adenosine A_1 receptors expressed in human CHO cells. [c] Displacement of specific [3]ZM2421385 binding in adenosine A_{2A} receptors expressed in human HeLa cells. [d] Displacement of specific [^{3}H]DPCPX binding in human HEK-293 cells. [e] Displacement of specific [^{3}H]NECA binding in adenosine A_3 receptors expressed in human HeLa cells.

compounds that can be almost as active as their counterparts in subset **I** (R_5 = CO_2R, e.g. compare compound **20** with **108**), something that is well captured by the FEP calculations (see Supporting Information S1). The systematic drop in affinity observed when an amide function replaces the ester in R_5 (subset **V**) is also correctly reproduced in our models, with calculated loss in affinity close to or higher than the experimental threshold of the binding experiment (e.g. $\Delta\Delta G_{exp} \geq 3.27$ kcal/mol, see Tables S1−S3), indicating that this function does not fit on the designated binding site. The same applies for the phosphate and oxazolyl containing compounds (series **VII** and **VIII**), and in the former case, the ligand cannot even be accommodated in the binding site to run any FEP calculation.

Finally, the extensive exploration of the alkoxy substituent on the ester function resulted in a broad range of effects in affinity, as illustrated Figure 7, showing a bar plot representation of the experimental affinities within subsets **I** and **IX**. This effect is, in most cases, correctly reproduced and rationalized by FEP simulations, particularly in the 3-furyl (Supporting Information S2) and 3-thienyl (Supporting Information S3) containing compounds. The structural reason of the observed effects can be traced back to the presence of two buried water molecules adjacent to the hydrophobic pocket (see Figure 8B,C), which were previously characterized as highly stable.[67] Indeed, along the MD simulations associated to the FEP calculations, the compounds with bulkier alkyl chains at R_5 = CO_2R trend to selectively displace one or the two water molecules (depicted as water 2 and 3 in Figure 8) as compared to compounds with optimized R chains, which only displace the unstable water 1 (see Figure 8). The overall agreement of our FEP calculations and experiment is very reasonable, with a MAE of 1.15 kcal/mol for all perturbations with measurable experimental binding affinities, which fall well within values previously reported by others on homology models with much smaller datasets and provide a better signal for the described SAR observations than more intuitive relationships, such as correlation of affinity shifts with MW or SASA of the substituent in R_5 (data not shown). Altogether, the experimental data and computational modelling suggest a combined effect due to the optimal shape complementarity and specific water displacement elicited by the R_5 substituent, which is also dependent on the positioning of the heteroatom within the ring at R_4.

Preliminary ADME Exploration. With the aim to early identify metabolic liabilities of herein explored series, the inhibitory activity of (±)-**38** and (±)-**47** at two prototypical cytochrome P450 isoforms (CYP3A4 and CYP2D6) was assessed.[68] The selected subfamilies (CYP3A4 and CYP2D6) are abundant in the liver, shows broad substrate specificity, and are responsible for the metabolization of numerous drugs.[69−71] This data would enable to anticipate potential side effects and to examine the tendency for drug−drug interactions. The assays (done in duplicates) use fluorescence-based detection and employed 7-benzyloxy-4-(trifluoromethyl)-coumarin (IC_{50} = 0.008 μM), ketoconazole (IC_{50} = 0.027 μM), and quinidine (IC_{50} = 0.0073 μM) as references for CYP3A4 and CYP2D6. The obtained data is presented in Table 10. As observed, at the evaluated concentrations (1 and 10 μM), ligands (±)-**38** and (±)-**47** do not show substantial interaction with the studied cytochrome isoforms (CYP3A4 and CYP2D6). The ADME profile (in vitro) of the novel potent A_{2B} antagonists herein identified (**38** and **47**) was completed by evaluating its stability in human microsomes. The obtained data revealed that both ligands exhibited satisfactory microsomal stability, with 65 and 77% of (±)-**38** and (±)-**47** remaining unaltered after 60 min of exposure to human microsomes. The emerging ADME data highlight the attractiveness of the identified lead compounds.

https://dx.doi.org/10.1021/acs.jmedchem.0c01431
J. Med. Chem. 2021, 64, 458−480

Table 8. Structure and Binding Data for the 3,4-Dihydropyridin-2(1*H*)-ones 153−180 at the hARs (Subset IX, Figure 2)

Compound	R_4	R_5	K_i (nM) or % at 1 μM[a]			
			hA_1[b]	hA_{2A}[c]	hA_{2B}[d]	hA_3[e]
153	2-furyl		2%	3%	35%	1%
154	2-furyl		6%	1%	84.3 ± 2.1	3%
155	2-furyl		19%	41%	95.1 ± 2.4	1%
156	2-furyl		1%	23%	577 ± 23	14%
157	2-furyl		1%	5%	1%	4%
158	2-furyl		29%	36%	138 ± 4	1%
159	2-furyl		42%	22%	561 ± 34	1%
160	3-furyl		17%	2%	28%	5%
161	3-furyl		13%	1%	201 ± 8	11%
162	3-furyl		20%	32%	307 ± 10	1%
163	3-furyl		6%	1%	1008 ± 37	1%
164	3-furyl		15%	3%	4%	1%
165	3-furyl		29%	43%	426 ± 17	3%
166	3-furyl		46%	25%	739 ± 32	2%
167	2-thienyl		13%	4%	6%	1%
168	2-thienyl		5%	2%	7%	7%
169	2-thienyl		24%	26%	1094 ± 19	2%
170	2-thienyl		9%	20%	1%	1%
171	2-thienyl		7%	14%	3%	1%
172	2-thienyl		23%	27%	1572 ± 102	1%
173	2-thienyl		39%	22%	2842 ± 59	1%
174	3-thienyl		22%	1%	26%	6%
175	3-thienyl		5%	1%	39%	7%
176	3-thienyl		40%	41%	405 ± 11	3%
177	3-thienyl		5%	1%	659 ± 23	5%
178	3-thienyl		8%	2%	4%	1%
179	3-thienyl		39%	46%	724 ± 87	3%
180	3-thienyl		48%	32%	1041 ± 33	2%
ISAM-140	-	-	20%	25%	3.49 ± 0.2	2%
ZM241385	-	-	683 ± 4	1.9 ± 0.1	65.7 ± 1.7	863 ± 4
DPCPX	-	-	2.20 ± 0.2	157 ± 2.9	73.24 ± 2.0	1722 ± 11

[a] $n = 3$ for K_i values, or $n = 2$ for percentage displacement of specific binding. [b] Displacement of specific [^{3}H]DPCPX binding in adenosine A_1 receptors expressed in human CHO cells. [c] Displacement of specific [3]ZM2421385 binding in adenosine A_{2A} receptors expressed in human HeLa cells. [d] Displacement of specific [^{3}H]DPCPX binding in human HEK-293 cells. [e] Displacement of specific [^{3}H]NECA binding in adenosine A_3 receptors expressed in human HeLa cells.

Evaluation of the Antimetastatic Effect. It is well accepted that A_{2B}AR activation has to play a crucial role in promoting cell migration and motility[32,72] and also in early events of the multistep process of cell invasion and metastasis.[25,30,73] In addition, adenosine binding to A_{2B}AR on tumor cells enhance their metastatic capabilities, while A_{2B}AR activation enhances tumor chemotaxis and metastasis in animal models of melanoma and breast cancer.[9,74,75] These precedents aimed us to briefly investigate a potential antimetastatic effect of the most appealing ligands identified in this work on three representative PCa cell lines (LNCaP, PC-3, and DU145). The selected ligands were tested as racemates [(±)-**38** and (±)-**47**]. Elected cell lines are derived from PCa metastasis (isolated from the lymph nodes, bone, and brain, respectively) and represent states with different metastatic potential and androgen responses. To rule out the potential cytotoxic effect of (±)-**38** or (±)-**47** in LNCaP, PC-3, and DU145, the cell growth inhibitory activity of these ligands was preliminarily evaluated. Both compounds were tested (10 and 100 μM) following described protocols (MTT assays) using cisplatin as the control.[76,77] These experiments unequivocally confirmed that (±)-**38** or (±)-**47** do not exhibit a cytotoxic effect at the tested concentrations. The transwell migration assay[78] was used as a marker of A_{2B}AR antimetastatic activity. The cytopathic changes induced by selected compounds in the PC-3 cell line were analyzed using confocal microscopy.[79] For the sake of comparison, the prototypic A_{2B}AR antagonist **PSB603**[34] was also included in

https://dx.doi.org/10.1021/acs.jmedchem.0c01431
J. Med. Chem. 2021, 64, 458−480

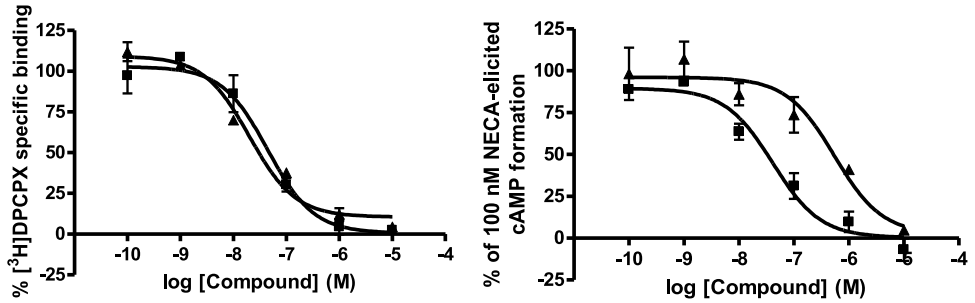

Figure 3. Radioligand binding and functional assays. (Left) Concentration−response curves of **47** (▲) and **38** (■) at hA_{2B} ARs labeled with 22 nM [^{3}H]DPCPX. (Right) Concentration−response curves of **47** (▲) and **38** (■) over 100 nM NECA-elicited cAMP formation. Points represent the mean ± SD (vertical bars) of three independent experiments.

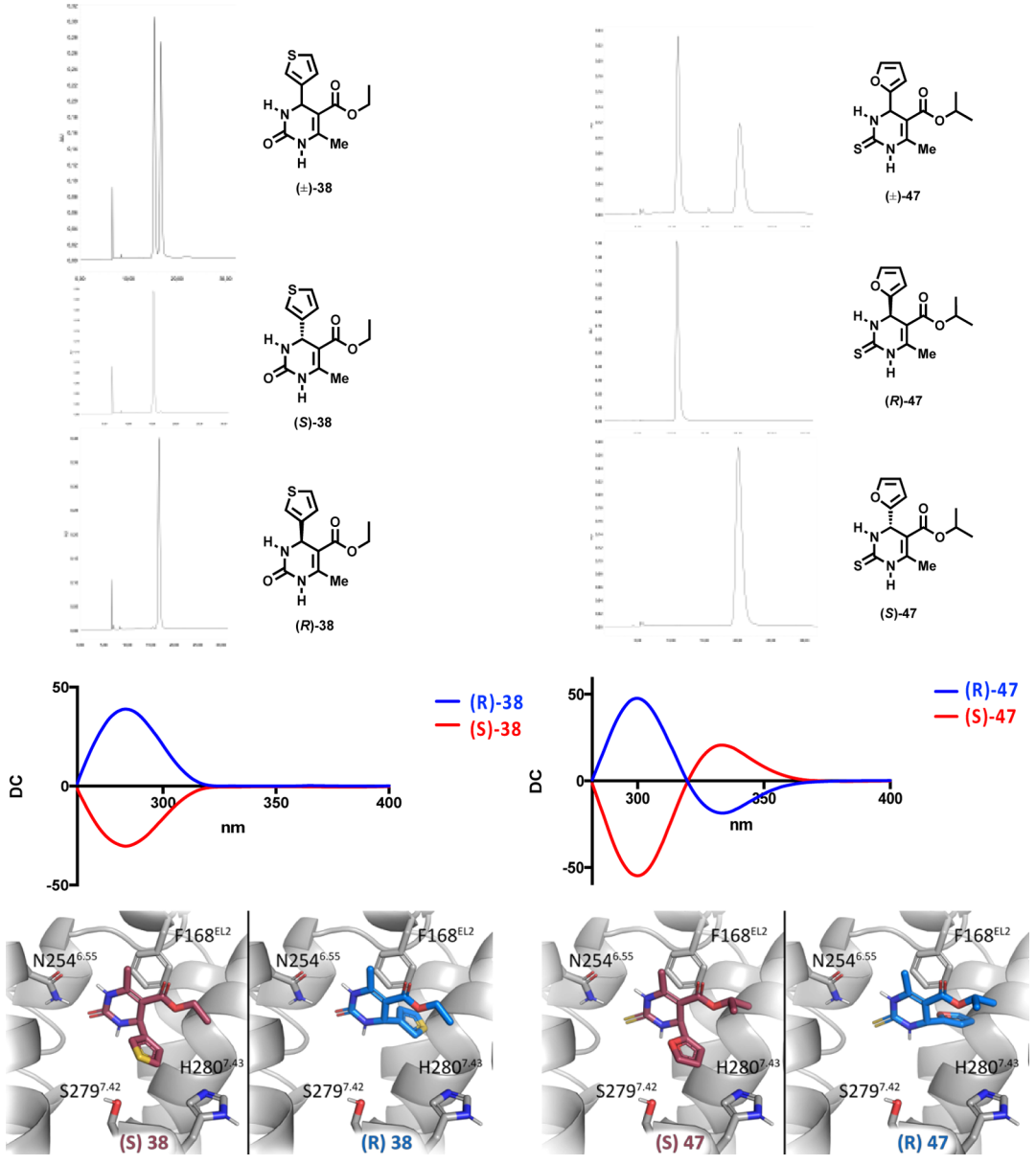

Figure 4. Chiral HPLC traces, CD spectra, and absolute configuration for (±)-**38** and (±)-**47** and its enantiomers.

the study. Figure 9 shows the results of the transwell migration assay after 72 h of exposure to (±)-**38**, (±)-**47**, and **PSB603** (at their respective K_i values) compared to untreated cells (controls). As observed, the optimized 3,4-dihydropyridine derivatives (±)-**38** and (±)-**47** significantly ($p < 0.05$) decreased PC-3, DU145, and LNCaP cells migration in comparison to controls (Figure 9A). Moreover, the antimigratory effect of this pair of ligands is indeed

https://dx.doi.org/10.1021/acs.jmedchem.0c01431
J. Med. Chem. 2021, 64, 458−480

Table 9. Structure and Binding Data for the Enantiomers of the 3,4-Dihydropyridin-2(1*H*)-ones/thiones 38 and 47 at the hARs

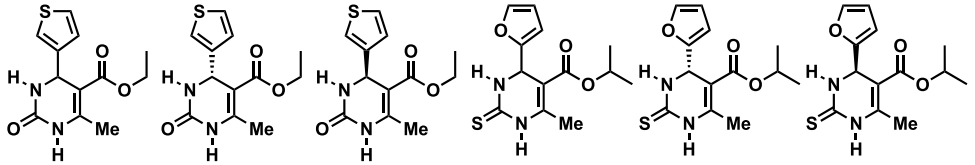

(±)-38 (*S*)-38 (*R*)-38 (±)-47 (*S*)-47 (*R*)-47

			K_i (nM) or % at 1 μM			
compound	R_4	R_5	hA_1[a] (%)	hA_{2A}[b] (%)	hA_{2B}[c]	hA_3[d] (%)
(±)-**38**	3-thienyl	Et	16	34	23.6 ± 1.0	11
(*R*)-**38**	3-thienyl	Et	5	21	19%	3
(*S*)-**38**	3-thienyl	Et	10	9	11.1 ± 1.4	6
(±)-**47**	2-furyl	*i*-Pr	15	18	10.2 ± 0.5	1
(*R*)-**47**	2-furyl	*i*-Pr	10	6	12%	2
(*S*)-**47**	2-furyl	*i*-Pr	8	13	6.30 ± 1.1	1

[a] n = 3 for K_i values, or n = 2 for percentage displacement of specific binding. [b] Displacement of specific [^{3}H]DPCPX binding in adenosine A_1 receptors expressed in human CHO cells. [c] Displacement of specific [3]ZM2421385 binding in adenosine A_{2A} receptors expressed in human HeLa cells. [d] Displacement of specific [^{3}H]DPCPX binding in human HEK-293 cells. [e] Displacement of specific [^{3}H]NECA binding in adenosine A_3 receptors expressed in human HeLa cells.

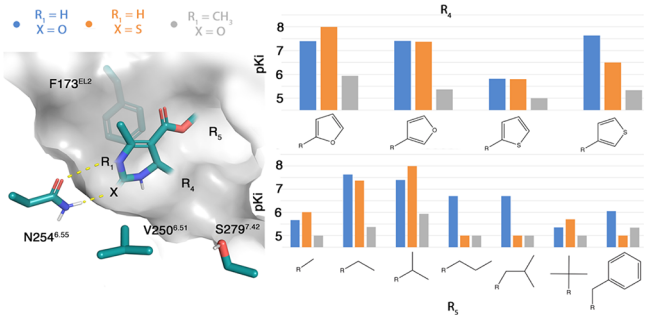

Figure 5. Proposed binding mode of the 3,4-dihydropyrimidin-2(1*H*)-one/thione scaffold (left) and graphical analysis of the SAR from tables **I**–**III** (right). The bars represent the pK_i value on the A_{2B}AR for the highest affinity compound within each of the R_4 (top graph) or R_5 (bottom graph) substituents, as extracted from each of the three subsets (blue: subset **I**, compounds **16**–**43** in Table 1; orange, subset **II**, compounds **44**–**71** in Table 2; gray, subset **III**, compounds **72**–**99** in Table 3).

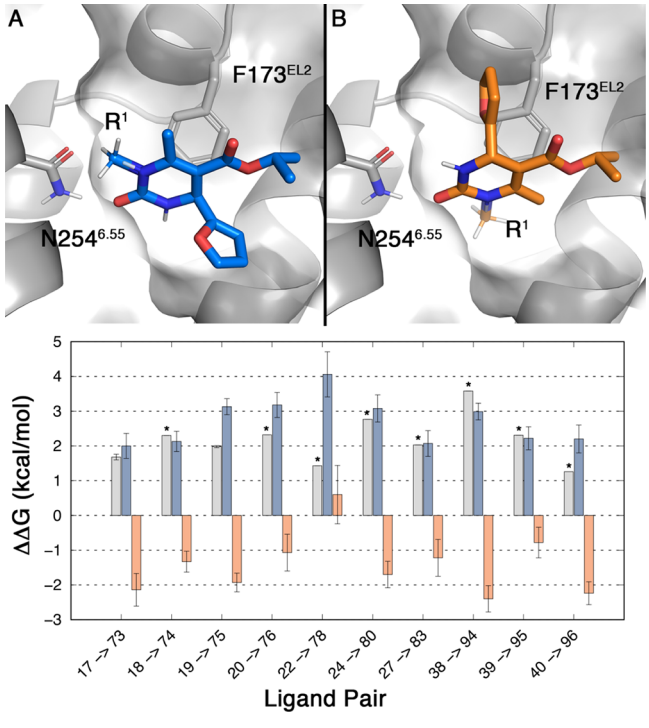

Figure 6. Effect of methylation on R_1. The binding modes considered are depicted in panels (A,B) for the compound pair **19** (R_1 = NH) and **75** (R_1 = N–CH_3). Panel (C) depicts the result of the FEP simulations, performed on each binding pose for 10 pairs of compounds. Color code corresponds to the binding pose, blue for pose A, and orange for pose B. * = no detectable binding.

superior to that observed for **PSB603** (Figure 9A). Interestingly, the antimetastatic effect was in all cases lightly superior on PC-3 cells compared to DU145 and LNCaP. Here, the antimigratory activity of ligand (±)-**47** was clearly superior to ligand (±)-**38** (50 vs 35% in PC-3 migration assay), which correlates with the observed structural and affinity differences between the two ligands.

Cytopathic changes are considered an indicator of tumor progression,[80,81] and these changes are usually employed to evaluate the anti-invasive effect of antitumoral compounds.[79−82] It is already known that migration is comparatively faster in PC-3 cells that have an elongated shape compared to rounded ones.[80] Changes in the morphology may be driven by modification in the actin cytoskeleton organization and this, in turn, can target cell motility.[81,82] As a complement of the previous data, it was decided to study the cytopathic changes induced by the herein developed pyrimidin-2-ones [(±)-**38** and (±)-**47**] and the reference ligand **PSB603** in PC-3 cells using confocal laser scanning microscopy.[79−82]

As depicted in Figure 10, PC-3 cells treated with ligands (±)-**38** or (±)-**47** exhibited a rounded shape as the predominant phenotype and showed actin skeleton reorganization. Similarly, cells treated with **PSB603** showed similar changes. In contrast, untreated PC-3 cells (control) showed an elongated morphology and ellipsoid nuclei with eu- and hetero-chromatin; actin filaments localized mainly beneath the plasma membrane and carboxyfluorescein diacetate succini-

https://dx.doi.org/10.1021/acs.jmedchem.0c01431
J. Med. Chem. 2021, 64, 458−480

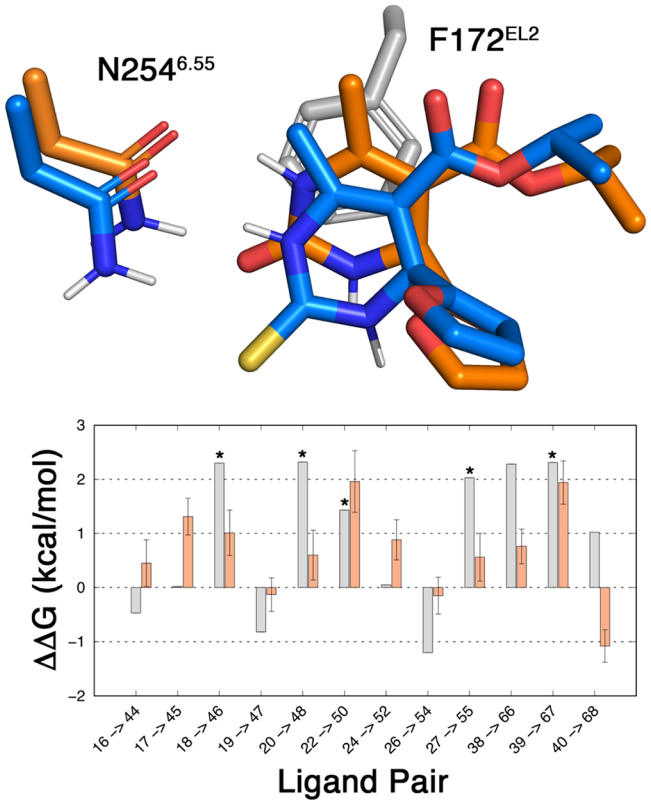

Figure 7. Binding mode of compounds **19** (subset **I**, orange) and **47** (subset **II**, blue), before and after the corresponding FEP transformation in the A_{2B}AR model (top). It can be appreciated by the shift in the binding orientation due to the heteroatom change. Experimental and calculated binding free energies between this and analogous compound pairs in subsets **I** and **II** are depicted in the bar graph (bottom). *No detectable binding.

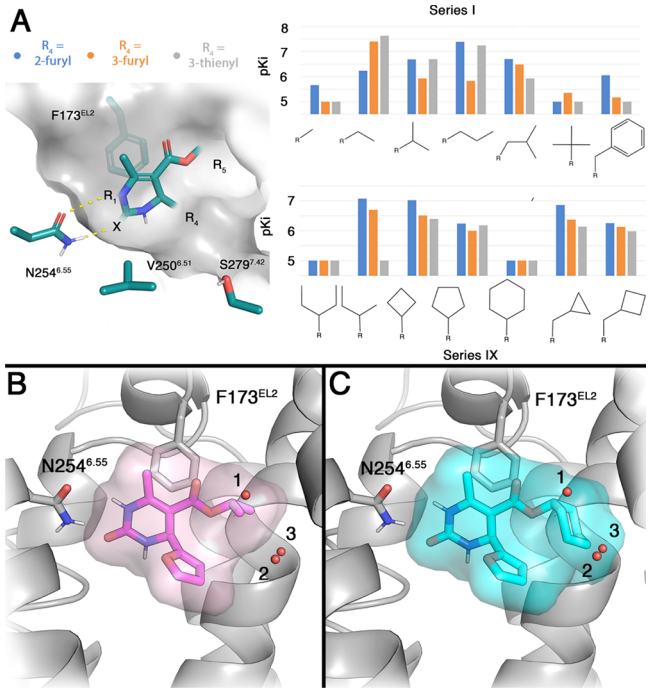

Figure 8. (A) Proposed binding mode of the 3,4-dihydropyrimidin-2-one scaffold (left) and graphical analysis of the SAR from tables **I** and **IX** (right). The bars represent the pK_i value for each of the R_5 substituents, for the three groups of R_4 with the highest affinity [2-furyl (blue), 3-furyl (orange), and 3-thienyl (gray)]. Binding mode of **19** (B, in pink) and **157** (C, in blue), binding site waters (from apo MD simulations) are depicted in spheres. Water 1 is replaced by both compounds; however, waters 2 and 3 are not displaced by **19** (**SYAF014**). These waters are buried deeply in the binding site and overlay with structural waters from the A_{2A}AR crystal structure (PDB: 4EIY). It is likely that these waters are favorably accommodated in the binding site and hence should not be displaced by any compound, in agreement with the decrease in affinity of **157** compared to **19**.

midyl ester (CFDA-SE) stained homogenously the cytoplasm (Figure 9). The excellent antimigratory effect of (±)-**47** and (±)-**38** supports the antimetastatic effect observed. These experiments additionally evidenced their superior efficacy on PC-3 cell lines and the higher antimetastatic profile of (±)-**47**. The outstanding antimigratory effect documented herein for optimized ligands suggests that they could be attractive pharmacological tools to explore potential applications of A_{2B}AR antagonists in the implementation of novel approaches to cancer treatment.

CONCLUSIONS

In summary, we have disclosed a large library of 3,4-dihydropyrimidin-2(1*H*)-ones as potent and selective A_{2B}AR ligands and confirmed its functional (antagonistic) behavior through cAMP assays. The biological dataset enabled the comprehensive examination of the most prominent features of the SAR and SSR in this series. The SAR trends were complemented and interpreted with a comprehensive computational modeling analysis based on rigorous FEP simulations, starting from the receptor-driven docking model that initially guided the design of these series. The combined use of preparative chiral HPLC and CD enabled to obtain experimental evidences supporting the stereospecific interaction between the different stereoisomers of the most attractive hA_{2B}AR antagonists identified herein. An exploratory ADME study of optimized A_{2B} antagonists evidenced the insignificant inhibitory effect at CYP3A4 and CYP2D6 and to corroborate its microsomal stability. The antimetastatic effect of 3,4-dihydropyrimidin-2(1*H*)-ones **47** and **38** was preliminarily validated in vitro in two androgen-insensitive (PC-3 and DU145) and one androgen-sensitive (LNCaP) prostate cancer cells. These results support a promising future for A_{2B}AR antagonists in the context of emerging therapeutic approaches for cancer treatment.

EXPERIMENTAL SECTION

Chemistry. Unless otherwise indicated, all starting materials, reagents, and solvents were purchased and used without further purification. After extraction from aqueous phases, the organic solvents were dried over anhydrous sodium sulfate. The reactions were monitored by thin-layer chromatography (TLC) on 2.5 mm Merck silica gel GF 254 strips, and the purified compounds each showed a single spot; unless stated otherwise, UV light and/or iodine vapor were used to detect compounds. The Biginelli reactions were performed in coated Kimble vials on a PLS (6 × 4) organic synthesizer with orbital stirring. The purity and identity of all tested compounds were established by a combination of HPLC, elemental analysis, mass spectrometry, and NMR spectroscopy as described below. Purification of isolated products was carried out by column chromatography (Kieselgel 0.040−0.063 mm, E. Merck) or medium pressure liquid chromatography on a CombiFlash Companion (Teledyne ISCO) with RediSep pre-packed normal-phase silica gel

https://dx.doi.org/10.1021/acs.jmedchem.0c01431
J. Med. Chem. 2021, 64, 458−480

Table 10. Inhibition Data of (±)-38 and (±)-47 on CYP3A4 and CYP2D6[a]

	CYP3A4 (BFC) % inhibition		CYP3A4 (DBF) % inhibition		CYP2D6 % inhibition	
cmpd	(1 μM) (%)	(10 μM) (%)	(1 μM) (%)	(10 μM) (%)	(1 μM) (%)	(10 μM) (%)
(±)-**38**	15	44	4	12	15	22
(±)-**47**	1	13	3	1	15	12

[a]Presented data are the mean ± SD of three (n = 3) experiments. The percentage of inhibition (at 1 and 10 μM) is described due to the negligible effect of the compounds at both cytochromes.

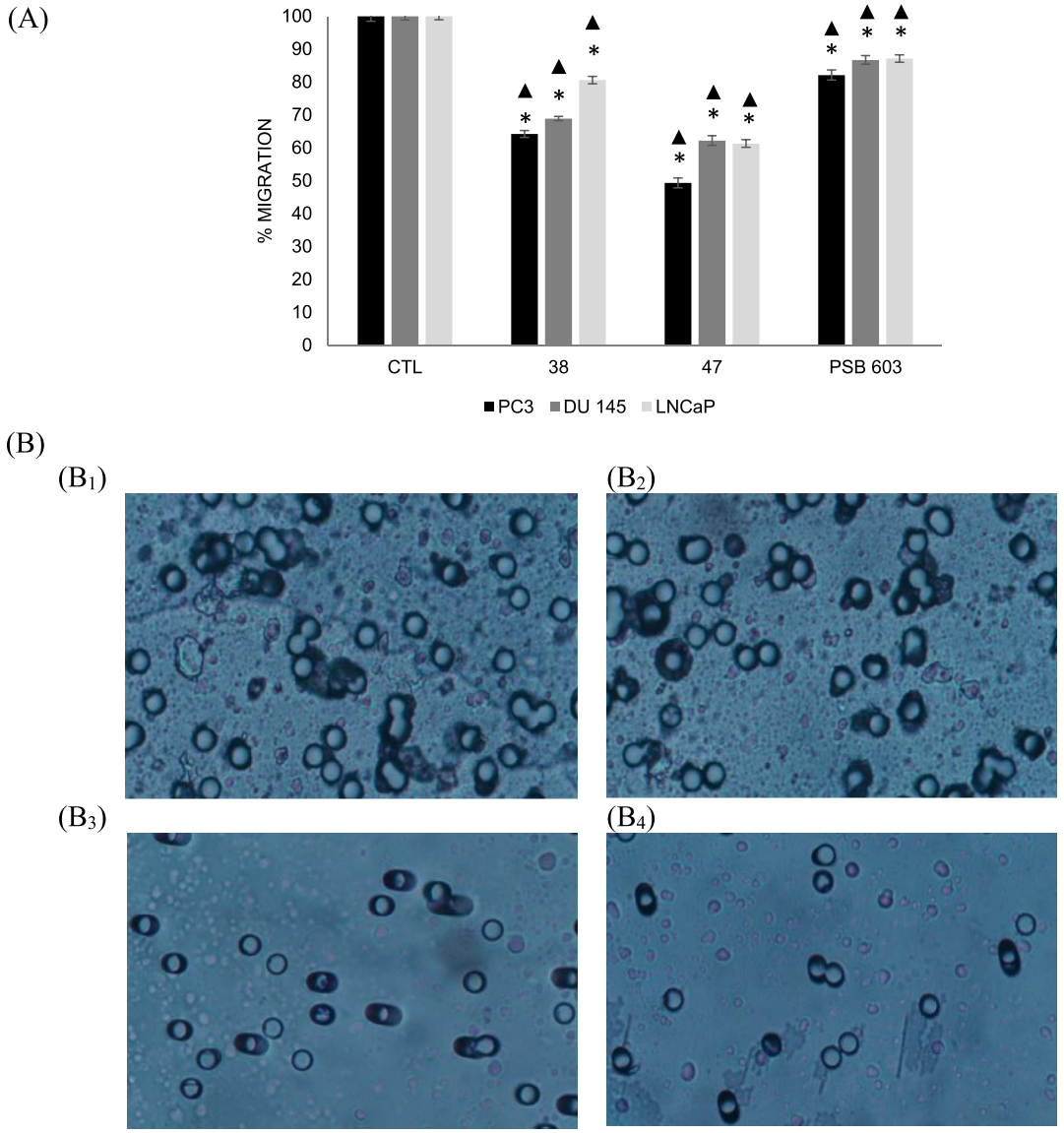

Figure 9. Migration of PC-3, DU145 and LNCaP cells. (A) A_{2B}AR antagonists (±)-**38** and (±)-**47** inhibited PC-3, LNCaP, and DU145 cell migration, in comparison to the controls (CTL) and **PSB603**. Results are expressed as mean ± SE, from at least three separate experiments, each conducted in triplicates. *A_{2B}AR antagonists' treatment was significantly different compared with control treatment ($p < 0.05$); ▲A_{2B}AR antagonist (±)-**38** and A_{2B}AR antagonist (±)-**47** were significantly different compared with A_{2B}AR antagonist **PSB603** ($p < 0.05$). (B) Representative microphotographs of PC-3 cells (40×) which migrated through the chamber membranes: (B_1) control, (B_2), A_{2B}AR antagonist **PSB603**, (B_3) A_{2B}AR antagonist (±)-**38**, (B_4) A_{2B}AR antagonist (±)-**47**.

(35−60 μm) columns followed by recrystallization. Melting points were determined on a Gallenkamp melting point apparatus and are uncorrected. The NMR spectra were recorded on Bruker AM300 and XM500 spectrometers. Chemical shifts are given as δ values against tetramethylsilane as the internal standard, and J values are given in Hz. Mass spectra were obtained on a Varian MAT-711 instrument. High-resolution mass spectra were obtained on an Autospec Micromass spectrometer. Analytical HPLC was performed on an Agilent 1100 system using an Agilent Zorbax SB-Phenyl, 2.1 mm × 150 mm, 5 μm column with gradient elution using the mobile phases (A) H_2O containing 0.1% CF_3COOH and (B) MeCN and a flow rate of 1 mL/min. The purity of all tested compounds was determined to be >95%. The structural and spectroscopic data obtained for all compounds described is provided in the Supporting Information.

https://dx.doi.org/10.1021/acs.jmedchem.0c01431
J. Med. Chem. 2021, 64, 458−480

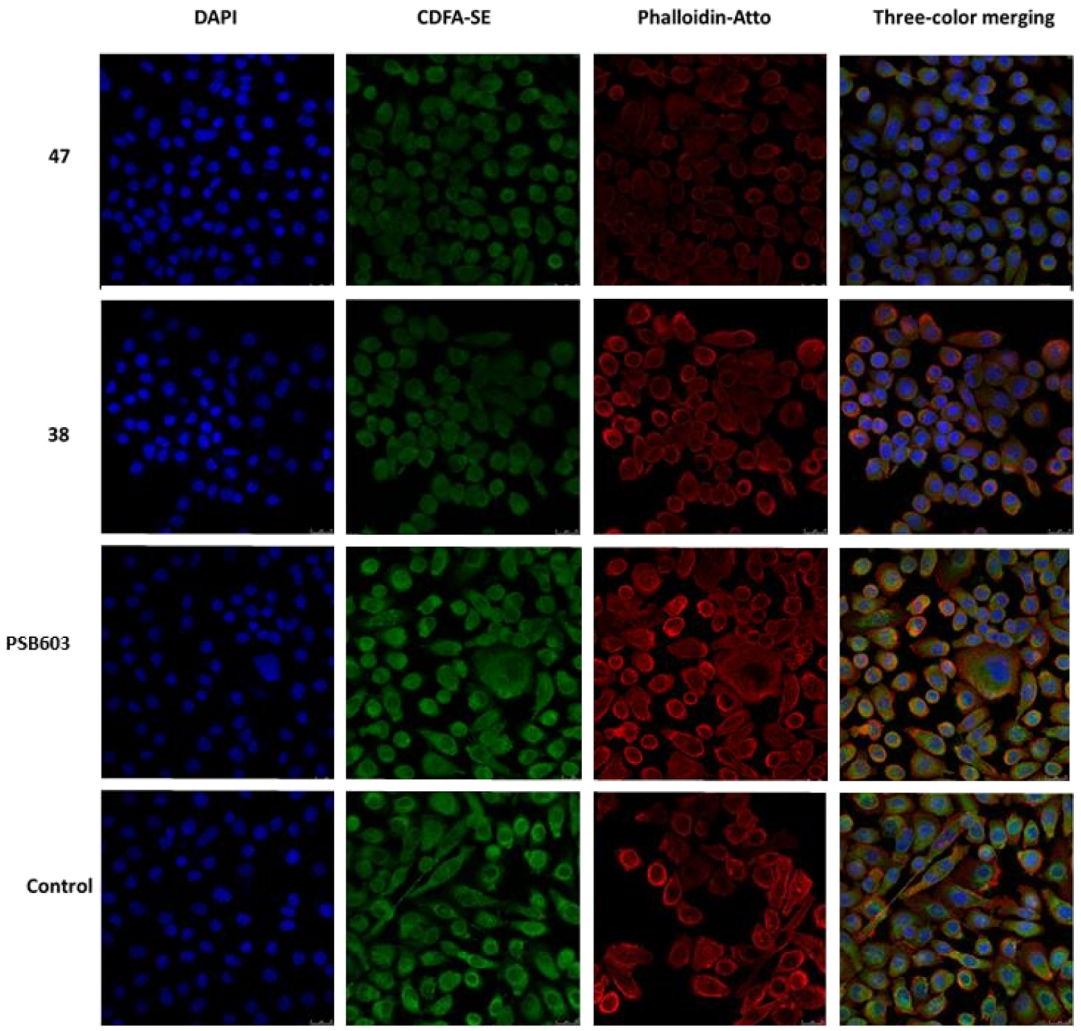

Figure 10. Cytopathic changes of PC-3 cells observed by confocal laser scanning microscopy. Blue (DAPI), green (CFDA-SE), and red (phalloidin−ATTO 647N) and merge of three channels. Cells treated with (±)-**47** (10.2 nM) or (±)-**38** (23.6 nM) showed predominantly rounded shape phenotype with DNA condensation. Untreated PC-3 cells showed an elongated phenotype with cytoplasmic projections when compared with A_{B2}AR antagonist-treated PC-3 cells.

The chiral resolution of selected racemic ligands [(±)-**38** and (±)-**47**] was performed using a Water Breeze 2 (binary pump 1525, detector UV/visible 2489, 7725i Manual Injector Kit 1500 Series) with a 250 mm × 10 mm Lux 5 μm amylose-2 (Phenomenex) using a linear gradient of the mobile phase (*n*-hexane/*i*-propanol) at 25 °C. A detailed description of the experimental protocols and relevant parameters (retention times and stereochemical purities) is provided in the Supporting Information. All single stereoisomers were isolated, and their stereochemical purity was analyzed by chiral HPLC (>97% for each stereoisomer) and then characterized by NMR in $CDCl_3$. CD spectra were recorded on a Jasco-815 system equipped with a Peltier-type thermostatic accessory (CDF-426S, Jasco). Measurements were carried out at 20 °C using a 1 mm quartz cell in a volume of 300−350 mL. Compounds (0.1 mg) were dissolved in MeOH (1.0 mL). The instrument settings were bandwidth, 1.0 nm; data pitch, 1.0 nm; speed, 500 nm/min; accumulation, 10; and wavelengths, 400−190 nm.

General Procedure for the Biginelli Synthesis of 3,4-Dihydropyrimidin-2(1*H*)-ones (16−43) and 3,4-Dihydropyrimidin-2(1*H*)-thiones (44−71). A mixture of urea **13a** or thiourea **13b** (7.5 mmol), aldehyde **14a−d** (5 mmol), the β-ketoester **15a−g** (5 mmol), and $ZnCl_2$ (0.5 mmol) in 3 mL of tetrahydrofuran (THF) in coated Kimble vials was stirred with orbital stirring at 80 °C for 12 h. After completion of the reaction, as indicated by TLC, the reaction mixture was poured onto crushed ice and stirred for 5−10 min. The solid separated was filtered under suction, washed with ice-cold water (20 mL), and then purified either by recrystallization or column chromatography on a silica gel.

General Procedure for the Biginelli Synthesis of 3,4-Dihydropyrimidin-2(1*H*)-ones (72−99). A mixture of methylurea **13c** (7.5 mmol), aldehyde **14a−d** (5 mmol), the β-ketoester **15a−g** (5 mmol), and H_3BO_3 (0.5 mmol) in 3 mL of THF in coated Kimble vials was stirred with orbital stirring at 80 °C for 12 h. After completion of the reaction, as indicated by TLC, the reaction mixture was poured onto crushed ice and stirred for 5−10 min. The solid separated was filtered under suction, washed with ice-cold water (20 mL), and then purified either by recrystallization or column chromatography on a silica gel.

General Procedure for the Biginelli Synthesis of 3,4-Dihydropyrimidin-2(1*H*)-ones (105−120). A mixture of the urea **13a** (7.5 mmol), aldehyde **14a−d** (5 mmol), the 1,3-diketone **100a−d** (5 mmol), and AcOH (0.5 mmol) in 3 mL of THF in coated Kimble vials was stirred with orbital stirring at 80 °C for 12 h. After completion of the reaction, as indicated by TLC, the reaction mixture was poured onto crushed ice and stirred for 5−10 min. The solid separated was filtered under suction, washed with ice-cold water (20 mL), and then purified either by recrystallization or column chromatography on a silica gel.

General Procedure for the Biginelli Synthesis of 3,4-Dihydropyrimidin-2(1*H*)-ones (121−136). A mixture of the

https://dx.doi.org/10.1021/acs.jmedchem.0c01431
J. Med. Chem. 2021, 64, 458−480

urea **13a** (7.5 mmol), aldehyde **14a−d** (5 mmol), the ketoamide **101a−d** (5 mmol), and $ZnCl_2$ (0.5 mmol) in 3 mL of THF in coated Kimble vials was stirred with orbital stirring at 80 °C for 12 h. After completion of the reaction, as indicated by TLC, the reaction mixture was poured onto crushed ice and stirred for 5−10 min. The solid separated was filtered under suction, washed with ice-cold water (20 mL), and then purified either by recrystallization or column chromatography on a silica gel.

General Procedure for the Biginelli Synthesis of 3,4-Dihydropyrimidin-2(1*H*)-ones (137−144). A mixture of the urea **13a** (7.5 mmol), aldehyde **14a−d** (5 mmol), the ketothioester **102a−b** (5 mmol) and $CeCl_3$ (0.5 mmol) in 3 mL of THF in coated Kimble vials was stirred with orbital stirring at 80 °C for 12 h. After completion of the reaction, as indicated by TLC, the reaction mixture was poured onto crushed ice and stirred for 5−10 min. The solid separated was filtered under suction, washed with ice-cold water (20 mL), and then purified either by recrystallization or column chromatography on a silica gel.

General Procedure for the Biginelli Synthesis of 3,4-Dihydropyrimidin-2(1*H*)-ones (145−148). A mixture of the urea **13a** (7.5 mmol), aldehyde **14a−d** (5 mmol), diethyl (2-oxopropyl)phosphonate **103** (5 mmol), and chloroacetic acid (0.5 mmol) in 3 mL of THF in coated Kimble vials was stirred with orbital stirring at 90 °C for 12 h. After completion of the reaction, as indicated by TLC, the reaction mixture was poured onto crushed ice and stirred for 5−10 min. The solid separated was filtered under suction, washed with ice-cold water (20 mL), and then purified either by recrystallization or column chromatography on a silica gel.

General Procedure for the Biginelli Synthesis of 3,4-Dihydropyrimidin-2(1*H*)-ones (149−152). A mixture of the urea **13a** (7.5 mmol), aldehyde **14a−d** (5 mmol), 1-(5-methyloxazol-2-yl)propan-2-one **104** (5 mmol), and $SnCl_2$ (0.5 mmol) in 3 mL of THF in coated Kimble vials was stirred with orbital stirring at 80 °C for 12 h. After completion of the reaction, as indicated by TLC, the reaction mixture was poured onto crushed ice and stirred for 5−10 min. The solid separated was filtered under suction, washed with ice-cold water (20 mL), and then purified either by recrystallization or column chromatography on a silica gel.

General Procedure for the Biginelli Synthesis of 3,4-Dihydropyrimidin-2(1*H*)-ones (153−180). A mixture of the urea **13a** (7.5 mmol), aldehyde **14a−d** (5 mmol), the β-ketoester **15h−n** (5 mmol), and $ZnCl_2$ (0.5 mmol) in 3 mL of THF in coated Kimble vials was stirred with orbital stirring at 80 °C for 12 h. After completion of the reaction, as indicated by TLC, the reaction mixture was poured onto crushed ice and stirred for 5−10 min. The solid separated was filtered under suction, washed with ice-cold water (20 mL), and then purified either by recrystallization or column chromatography on a silica gel.

Pharmacological Characterization. Radioligand binding competition assays were performed in vitro using hARs expressed in transfected HeLa [$hA_{2A}AR$ (9 pmol/mg protein) and hA_3AR (3 pmol/mg protein)], HEK-293 [$hA_{2B}AR$ (1.5 pmol/mg protein)], and CHO [hA_1AR (1.5 pmol/mg protein)] cells as described previously.[41−43,49] A brief description is given below. A_1AR competition binding experiments were carried out in membranes from CHO-A_1 cells labeled with 1 nM [^{3}H]DPCPX (K_D = 0.7 nM). Nonspecific binding was determined in the presence of 10 μM R-PIA. The reaction mixture was incubated at 25 °C for 60 min. $A_{2A}AR$ competition binding experiments were carried out in membranes from HeLa-A_{2A} cells labeled with 3 nM [^{3}H]ZM241385 (K_D = 2 nM). Nonspecific binding was determined in the presence of 50 μM NECA. The reaction mixture was incubated at 25 °C for 30 min. $A_{2B}AR$ competition binding experiments were carried out in membranes from HEK-293-A_{2B} cells (Euroscreen, Gosselies, Belgium) labeled with 25 nM [^{3}H]DPCPX (K_D = 21 nM). Nonspecific binding was determined in the presence of 400 μM NECA. The reaction mixture was incubated at 25 °C for 30 min. A_3AR competition binding experiments were carried out in membranes from HeLa-A_3 cells labeled with 10 nM [^{3}H]NECA (K_D = 8.7 nM). Nonspecific binding was determined in the presence of 100 μM R-PIA. The reaction mixture was incubated at 25 °C for 180 min. After the incubation time, membranes were washed and filtered, and radioactivity was detected in a MicroBeta Trilux reader (PerkinElmer).

Functional Experiments. cAMP assays were performed at human $A_{2B}ARs$ using a cAMP enzyme immunoassay kit (Amersham Biosciences). HEK-293 cells were seeded (10,000 cells/well) in 96-well culture plates and incubated at 37 °C in an atmosphere with 5% CO_2 in Eagle's medium nutrient mixture F-12 (EMEM F-12), containing 10% fetal calf serum and 1% L-glutamine. Cells were washed 3× with 200 μL of assay medium (EMEM-F12 and 25 mM *N*-(2-hydroxyethyl)piperazine-*N*′-ethanesulfonic acid pH = 7.4) and preincubated with assay medium containing 30 μM rolipram and test compounds at 37 °C for 15 min. 10 μM NECA was incubated for 15 min at 37 °C (total incubation time 30 min). Reaction was stopped with lysis buffer supplied in the kit, and the enzyme immunoassay was carried out for detection of intracellular cAMP at 450 nm in an Ultra Evolution detector (Tecan).

Data Analysis. IC_{50} values were obtained by fitting the data with nonlinear regression using Prism 5.0 software (GraphPad, San Diego, CA). For those compounds that showed either little affinity or poor solubility, a percentage inhibition of specific binding is reported. Results are the mean of three experiments (n = 3) each performed in duplicates.

In Vitro Migration Assay. The effects of (±)-**38**, (±)-**47**, and **PSB603** (23.6, 10.2, and 0.53 nM respectively) on PC-3, DU145, and LNCaP cell migration tests were assessed by using 24-well transwell cell culture chambers (6.5 mm diameter, 8.0 μm pore size, polycarbonate membrane) (Sigma-Aldrich, Madrid, MD, Spain) with Millicell Cell Culture Insert (Merck Millipore Madrid, MD, Spain).[67] In the upper chamber, 10^5 cells were seeded in 100 μL serum-free fetal bovine serum (FBS), while the lower chamber was filled with 600 μL of complete medium with 10% FBS. After 24 h of incubation, cells in the upper chamber were carefully removed with a cotton swab and cells that had migrated through the membrane and had stuck to the lower surface of the membrane were fixed with 4% paraformaldehyde (2 min) and stained with crystal violet stain (Sigma-Aldrich, Madrid, MD, Spain) (15 min). Stained cells were counted by photographing the membrane in five randomly selected fields using a microscope equipped with a digital camera (Olympus, Tokyo, Japan). At least three chambers from three different experiments were analyzed. Prostate adenocarcinoma cell lines PC-3, DU145, and LNCaP. PCa cells were cultured in RPMI 1640 supplemented with 10% FBS (Life Technologies, Madrid, MD, Spain), 100 U/mL penicillin, and 100 mg/mL streptomycin (penicillin−streptomycin solution 30-2300; LGC Standards Barcelona, CAT, Spain). All cells were maintained at 37 °C in a 5% CO_2 humidified incubator, grown to confluence, and thereafter seeded into well culture plates at assay-specific densities.

Migration Assay. As an indicator of the antimetastatic effect, we assessed PC-3, DU145, and LNCaP cell migration by using 24-well transwell cell culture chambers (6.5 mm diameter, 8.0 μm pore size, polycarbonate membrane) (cat. no. C6932; Sigma-Aldrich, Madrid, MD, Spain) with Millicell Cell Culture Insert (cat. no. PI8P01250; Merck Millipore Madrid, MD, Spain).[60] In the upper chamber, 10^5 cells were seeded in 100 μL serum-free FBS, while the lower chamber was filled with 600 μL of complete medium with 10% FBS. After 24 h of incubation, cells in the upper chamber were carefully removed with a cotton swab and cells that had migrated through the membrane and had stuck to the lower surface of the membrane were fixed with 4% paraformaldehyde (2 min) and stained with crystal violet stain (cat. no. C6158; Sigma-Aldrich, Madrid, MD, Spain) (15 min). Stained cells were counted by photographing the membrane in five randomly selected fields using a microscope equipped with a digital camera (Olympus, Tokyo, Japan). At least three chambers from three different experiments were analyzed. Migration was evaluated after 72 h of cell culture without or with each of the treatments tested.

Cell Morphological Changes by Scanning Confocal Microscopy. PC-3 cells were seeded in glass coverslips into incubation

https://dx.doi.org/10.1021/acs.jmedchem.0c01431
J. Med. Chem. 2021, 64, 458−480

chambers (24 h at 37 °C and 5% CO_2) in order to obtain full adherence. Thereafter, the medium was replaced with fresh complete medium containing antagonists **38** and **47**, or vehicles and plates were incubated for 72 h at 37 °C. Then, PC-3 cells were fluorescently stained for F-actin (phalloidin−ATTO 647N 1:500, cat. no. 65906; Sigma-Aldrich, Madrid, MD, Spain), nuclei (4′,6-diamidino-2-phenylindole, DAPI), and cytoplasm (CFDA-SE, cat. no. 1351201EDU; Bio-Rad Laboratories, Madrid, MD, Spain). The culture medium was replaced by PBS solution containing fluorescent dye CFDA-SE at 1 mM, and the cells were incubated 15 min. Subsequently, CFDA-SE solution was removed; cells were washed with PBS, fixed with 70% ethanol for 5 min, washed again with PBS, and finally, stained for with phalloidin−ATTO for 1 h. Then, the cells were washed with 0.9% sodium chloride (NaCl, cat. no. S7653; Sigma-Aldrich Madrid, MD, Spain) and stained with DAPI at 1 mg/mL for 10 min. Finally, slides were embedded in a VectaShield antifade mounting medium (cat. no. H-1000; Vector Laboratories, Burlingame CA, U.S.A.). The cells were analyzed with a Leica confocal microscope (Leica TCS SP5 II microscope).[79]

Receptor Modeling and Ligand Docking. Our computational strategy for the structure-based design of AR ligands involves a combination of homology modeling, ligand−receptor docking, and free energy calculations, as recently reviewed.[83] Homology modeling of and docking to the $hA_{2B}AR$: a 3D structure of the inactive form of the receptor was generated at the beginning of this project.[84] Briefly, the process consisted of the following sequential steps: (i) manual curation of the sequence alignment with the template $A_{2A}AR$ (PDB code 3EML),[66] (ii) generation and selection of homology models and loop refinement procedures with Modeler,[85] (iii) assessment of Asn/Gln/His rotamers and side chain protonation states with the MolProbity web server (http://molprobity.biochem.duke.edu/), and (iv) use of tools from the Schrödinger Suite for energetic structural refinements.[83] The previously described binding mode of **SYAF014**[64] in the $A_{2B}AR$ model was used as a starting point to manually dock all reported compounds within the series.

MD and FEP Calculations. The $hA_{2B}AR$ model obtained in the previous stage was inserted in the membrane and equilibrated under periodic boundary conditions using the PyMemDyn protocol described elsewhere.[86] Shortly, the starting structure is automatically embedded in a pre-equilibrated membrane consisting of 1-palmitoyl-2-oleoyl phosphatidylcholine lipids, with the TM bundle aligned to its vertical axis. This hexagonal-prism shaped box is then soaked with bulk water and energy minimized with GROMACS 4.6.[87] using the OPLS-AA force field[88] for protein and ligands, combined with the Berger parameters for the lipids.[89] The same setup is used for a 2.5 ns MD equilibration, where initial restraints on protein and ligand atoms are gradually released as described in detail in our original protocol.[86] The equilibrated binding site is then transferred to the MD software Q[90] for FEP calculations under spherical boundary conditions, using the automated QligFEP protocol.[91] A 25 Å sphere centered on the center of geometry of the ligand is considered for these MD simulations. Protein atoms in the boundary of the sphere (22−25 Å outer shell) had a positional restraint of 20 kcal/mol/Å^2, while solvent atoms were subject to polarization and radial restrains using the surface constrained all-atom solvent[90,92] model to mimic the properties of bulk water at the sphere surface. Atoms lying outside the simulation sphere are tightly constrained (200 kcal/mol/Å^2 force constant) and excluded from the calculation of nonbonded interactions. Long range electrostatic interactions beyond a 10 Å cut off were treated with the local reaction field method,[93] except for the atoms undergoing the FEP transformation where no cut-off was applied. Solvent bonds and angles were constrained using the SHAKE algorithm.[94] All titratable residues outside the sphere were neutralized, and histidine residues were assigned a hydrogen atom on the δ nitrogen. Residue parameters were translated from the OPLS-AA/M force field,[95] and the parameters for the ligand and lipids were inherited from the previous MD stage. The simulation sphere was warmed up from 0.1 to 298 K, during a first equilibration period of 0.61 ns, where an initial restraint of 25 kcal/mol/Å^2 imposed on all heavy atoms was slowly released for all complexes. Thereafter, the system was subject to 10 parallel replicates of unrestrained MD, where the FEP protocol is applied for each ligand transformation. Each of these MD replicates starts with a 0.25 ns unbiased equilibration period, with different initial velocities. Thereafter, the FEP protocol follows, which consists of 21 FEP λ-windows, distributed using a sigmoidal function and consisting of 10 ps each for every investigated ligand pair. In order to fulfil a thermodynamic cycle and calculate relative binding free energies, parallel FEP transformations are run in a sphere of water for each ligand pair. In these water simulations, the same parameters apply (i.e., sphere size, simulation time, etc.), and the relative binding free energy difference was estimated by solving the thermodynamic cycle utilizing the Bennett acceptance ratio.[96]

CYP3A4 and CYP2D6 Inhibition. The inhibitory activity of ligands (±)-**38** and (±)-**47** was assessed by following a published protocol.[68] Incubations were conducted in a 200 μL of volume in 96 well microtiter plates (COSTAR 3915). Addition of the cofactor-buffer mixture (KH_2PO_4 buffer, 1.3 mM NADP, 3.3 mM $MgCl_2$, 3.3 mM glucose-6-phosphate, and 0.4 U/mL glucose-6-phosphate dehydrogenase), supersomes control, and standard inhibitor (ketoconazole from Sigma-Aldrich) previously diluted and compounds to plates were carried out by a liquid handling station (Zephyr Caliper). The plate was then preincubated at 37 °C for 5 min, and the reaction initiated by the addition of prewarmed enzyme/substrate (E/S) mix. The E/S mix contained buffer (KH_2PO_4), c-DNA-expressed P450 in insect cell microsomes, substrate (DBF: dibenzylfluorescein), and other components to give the final assay concentrations in a reaction volume of 200 μL. Reactions were terminated after various times (a specific time for each cytochrome) by the addition of STOP solution [ACN/Tris-HCl 0.5 M 80:20 and NaOH 2 N for CYP3A4 (DBF)]. Fluorescence per well was measured using a fluorescence plate reader (Tecan Infinite M1000 Pro), and the percentage of inhibition was calculated.

Human Microsomal Stability. The human microsomes employed were purchased from Tebu-Xenotech. The A_{2B} antagonists [(±)-**38** and (±)-**47**] were incubated with the microsomes at 37 °C in a 50 mM phosphate buffer (pH = 7.4) containing 3 mM $MgCl_2$, 1 mM NADP, 10 mM glucose-6-phosphate, and 1 U/mL glucose-6-phosphate-dehydrogenase. Samples (75 μL) were taken from each well at 0, 10, 20, 40, and 60 min and transferred to a plate containing 4 °C 75 μL acetonitrile, and 30 μL of 0.5% formic acid in water was added for improving the chromatographic conditions. The plate was centrifuged (46,000*g*, 30 min), and supernatants were taken and analyzed in an UPLC−MS/MS (Xevo-TQD, Waters) by employing a BEH C18 column and an isocratic gradient of 0.1% formic acid in water/0.1% formic acid acetonitrile (60:40). The metabolic stability of the compounds was calculated from the logarithm of the remaining compounds at each of the time points studied.

■ ASSOCIATED CONTENT

Supporting Information

The Supporting Information is available free of charge at https://pubs.acs.org/doi/10.1021/acs.jmedchem.0c01431.

Molecular formula strings (CSV)

Peak summary report (PDF)

Computational chemistry; general information; general procedure for Biginelli synthesis; spectroscopic and analytical data for all compounds described; and analytical HPLC chromatograms of AF80 (38) and AF80 (47) (PDF)

■ AUTHOR INFORMATION

Corresponding Authors

José Brea − *Centro Singular de Investigación en Medicina Molecular y Enfermedades Crónicas (CIMUS), Universidade de Santiago de Compostela, 15782 Santiago de Compostela,*

https://dx.doi.org/10.1021/acs.jmedchem.0c01431
J. Med. Chem. 2021, 64, 458−480

Spain; Phone: +34 881815459; Email: pepo.brea@usc.es; Fax: +34-8818115474

Hugo Gutiérrez-de-Terán − *Department of Cell and Molecular Biology, Uppsala University, SE-75124 Uppsala, Sweden*; orcid.org/0000-0003-0459-3491; Phone: +46 18 471 5056; Email: hugo.gutierrez@icm.uu.se; Fax: +46 18 536971

Eddy Sotelo − *Centro Singular de Investigación en Química Biolóxica y Materiais Moleculares (CIQUS) and Departamento de Química Orgánica, Facultade de Farmacia, Universidade de Santiago de Compostela, 15782 Santiago de Compostela, Spain*; orcid.org/0000-0001-5571-2812; Phone: +34 881815732; Email: e.sotelo@usc.es; Fax: +34-881815704

Authors

María Majellaro − *Centro Singular de Investigación en Química Biolóxica y Materiais Moleculares (CIQUS) and Departamento de Química Orgánica, Facultade de Farmacia, Universidade de Santiago de Compostela, 15782 Santiago de Compostela, Spain*

Willem Jespers − *Department of Cell and Molecular Biology, Uppsala University, SE-75124 Uppsala, Sweden*; orcid.org/0000-0002-4951-9220

Abel Crespo − *Centro Singular de Investigación en Química Biolóxica y Materiais Moleculares (CIQUS) and Departamento de Química Orgánica, Facultade de Farmacia, Universidade de Santiago de Compostela, 15782 Santiago de Compostela, Spain*

María J. Núñez − *SNL, Departamento de Farmacología, Facultade de Medicina, Universidade de Santiago de Compostela, 15782 Santiago de Compostela, Spain*

Silvia Novio − *SNL, Departamento de Farmacología, Facultade de Medicina, Universidade de Santiago de Compostela, 15782 Santiago de Compostela, Spain*

Jhonny Azuaje − *Centro Singular de Investigación en Química Biolóxica y Materiais Moleculares (CIQUS) and Departamento de Química Orgánica, Facultade de Farmacia, Universidade de Santiago de Compostela, 15782 Santiago de Compostela, Spain*

Rubén Prieto-Díaz − *Centro Singular de Investigación en Química Biolóxica y Materiais Moleculares (CIQUS) and Departamento de Química Orgánica, Facultade de Farmacia, Universidade de Santiago de Compostela, 15782 Santiago de Compostela, Spain*; orcid.org/0000-0003-2539-3106

Claudia Gioé − *Centro Singular de Investigación en Química Biolóxica y Materiais Moleculares (CIQUS) and Departamento de Química Orgánica, Facultade de Farmacia, Universidade de Santiago de Compostela, 15782 Santiago de Compostela, Spain*

Belma Alispahic − *Department of Cell and Molecular Biology, Uppsala University, SE-75124 Uppsala, Sweden*

María I. Loza − *Centro Singular de Investigación en Medicina Molecular y Enfermedades Crónicas (CIMUS), Universidade de Santiago de Compostela, 15782 Santiago de Compostela, Spain*

Manuel Freire-Garabal − *SNL, Departamento de Farmacología, Facultade de Medicina, Universidade de Santiago de Compostela, 15782 Santiago de Compostela, Spain*

Carlota Garcia-Santiago − *SNL, Departamento de Farmacología, Facultade de Medicina, Universidade de Santiago de Compostela, 15782 Santiago de Compostela, Spain*

Carlos Rodríguez-García − *Centro Singular de Investigación en Química Biolóxica y Materiais Moleculares (CIQUS) and Departamento de Química Orgánica, Facultade de Farmacia, Universidade de Santiago de Compostela, 15782 Santiago de Compostela, Spain*

Xerardo García-Mera − *Departamento de Química Orgánica, Facultade de Farmacia, Universidade de Santiago de Compostela, 15782 Santiago de Compostela, Spain*

Olga Caamaño − *Departamento de Química Orgánica, Facultade de Farmacia, Universidade de Santiago de Compostela, 15782 Santiago de Compostela, Spain*

Christian Fernandez-Masaguer − *Departamento de Química Orgánica, Facultade de Farmacia, Universidade de Santiago de Compostela, 15782 Santiago de Compostela, Spain*

Javier F. Sardina − *Centro Singular de Investigación en Química Biolóxica y Materiais Moleculares (CIQUS), Universidade de Santiago de Compostela, 15782 Santiago de Compostela, Spain*; orcid.org/0000-0002-6758-0068

Angela Stefanachi − *Dipartimento di Farmacia-Scienze del Farmaco, Università degli Studi di Bari ALDO MORO, 70125 Bari, Italy*; orcid.org/0000-0002-9430-7972

Abdelaziz El Maatougui − *Centro Singular de Investigación en Química Biolóxica y Materiais Moleculares (CIQUS) and Departamento de Química Orgánica, Facultade de Farmacia, Universidade de Santiago de Compostela, 15782 Santiago de Compostela, Spain*

Ana Mallo-Abreu − *Centro Singular de Investigación en Química Biolóxica y Materiais Moleculares (CIQUS) and Departamento de Química Orgánica, Facultade de Farmacia, Universidade de Santiago de Compostela, 15782 Santiago de Compostela, Spain*

Johan Åqvist − *Department of Cell and Molecular Biology, Uppsala University, SE-75124 Uppsala, Sweden*; orcid.org/0000-0003-2091-0610

Complete contact information is available at: https://pubs.acs.org/10.1021/acs.jmedchem.0c01431

Author Contributions

[¶]M.M., W.J., and A.C. contributed equally to this work.

Notes

The authors declare no competing financial interest.

■ ACKNOWLEDGMENTS

This work was financially supported by the Consellería de Cultura, Educación e Ordenación Universitaria of the Galician Government: (grant: ED431B2017/70), Centro singular de Investigación de Galicia accreditation 2016−2019 (ED431G/09), Xunta de Galicia (ED431C 2018/21) and the European Regional Development Fund (ERDF), the Swedish Research Council (grant: 521-2014-2118), and by the Swedish strategic research program eSSENCE. The computations were performed on resources provided by the Swedish National Infrastructure for Computing (SNIC).

■ ABBREVIATIONS

ARs, adenosine receptors; $hA_{2B}R$, human A_{2B} adenosine receptors; $hA_{2A}R$, human A_{2A} adenosine receptors; CHO cells, Chinese hamster ovary cells; c-AMP, cyclic adenosine monophosphate; FEP, free energy perturbation; HPLC, high performance liquid chromatography; MAE, mean absolute

error; MD, molecular dynamics; MPLC, medium pressure liquid chromatography; NMR, nuclear magnetic resonance spectroscopy; PCa, prostate cancer; PC-3 and DU145, androgen-independent human prostate cancer cell line cell lines; PDB, Protein Data Bank; LNCaP, androgen-dependent human prostate cancer cell line cell line; SAR, structure−activity relationships; SEM, standard error of the mean; SCAAS, surface constrained all-atom solvent

REFERENCES

(1) Rivkees, S. A.; Reppert, S. M. RFL9 Encodes an A2b-Adenosine Receptor. *Mol. Endocrinol.* **1992**, *6*, 1598−1604.
(2) Pierce, K. D.; Furlong, T. J.; Selbie, L. A.; Shine, J. Molecular Cloning and Expression of an Adenosine A2b Receptor from Human Brain. *Biochem. Biophys. Res. Commun.* **1992**, *187*, 86−93.
(3) Beukers, M. W.; Den Dulk, H.; Van Tilburg, E. W.; Brouwer, J.; Ijzerman, A. P. Why Are A2B Receptors Low-Affinity Adenosine Receptors? Mutation of Asn273 to Tyr Increases Affinity of Human A2B Receptor for 2-(1-Hexynyl)adenosine. *Mol. Pharmacol.* **2000**, *58*, 1349−1356.
(4) Fredholm, B. B.; Irenius, E.; Kull, B.; Schulte, G. Comparison of the Potency of Adenosine as an Agonist at Human Adenosine Receptors Expressed in Chinese Hamster Ovary Cells. *Biochem. Pharmacol.* **2001**, *61*, 443−448.
(5) Fredholm, B. B.; Ijzerman, A. P.; Jacobson, K. A.; Linden, J.; Müller, C. E. International Union of Basic and Clinical Pharmacology. LXXXI. Nomenclature and Classification of Adenosine Receptors-An Update. *Pharmacol. Rev.* **2011**, *63*, 1−34.
(6) Yang, D.; Chen, H.; Koupenova, M.; Carroll, S. H.; Eliades, A.; Freedman, J. E.; Toselli, P.; Ravid, K. A New Role for the A2b Adenosine Receptor in Regulating Platelet Function. *J. Thromb. Haemostasis* **2010**, *8*, 817−827.
(7) Yang, D.; Koupenova, M.; McCrann, D. J.; Kopeikina, K. J.; Kagan, H. M.; Schreiber, B. M.; Ravid, K. The A2b Adenosine Receptor Protects against Vascular Injury. *Proc. Natl. Acad. Sci. U.S.A.* **2008**, *105*, 792−796.
(8) Yang, D.; Zhang, Y.; Nguyen, H. G.; Koupenova, M.; Chauhan, A. K.; Makitalo, M.; Jones, M. R.; St. Hilaire, C.; Seldin, D. C.; Toselli, P.; Lamperti, E.; Schreiber, B. M.; Gavras, H.; Wagner, D. D.; Ravid, K. The A2B Adenosine Receptor Protects against Inflammation and Excessive Vascular Adhesion. *J. Clin. Invest.* **2006**, *116*, 1913−1923.
(9) Morello, S.; Miele, L. Targeting the Adenosine A2b Receptor in the Tumor Microenvironment Overcomes Local Immunosuppression by Myeloid-Derived Suppressor Cells. *Oncoimmunology* **2014**, *3*, No. e27989.
(10) Vecchio, E. A.; Tan, C. Y. R.; Gregory, K. J.; Christopoulos, A.; White, P. J.; May, L. T. Ligand-Independent Adenosine A2B Receptor Constitutive Activity as a Promoter of Prostate Cancer Cell Proliferation. *J. Pharmacol. Exp. Ther.* **2016**, *357*, 36−44.
(11) Johnston-Cox, H.; Eisenstein, A. S.; Koupenova, M.; Carroll, S.; Ravid, K. The Macrophage A2b Adenosine Receptor Regulates Tissue Insulin Sensitivity. *PLoS One* **2014**, *9*, No. e98775.
(12) Sun, Y.; Huang, P. Adenosine A2B Receptor: From Cell Biology to Human Diseases. *Front. Chem.* **2016**, *4*, 37.
(13) Corset, V.; Nguyen-Ba-Charvet, K. T.; Forcet, C.; Moyse, E.; Chédotal, A.; Mehlen, P. Netrin-1-Mediated Axon Outgrowth and CAMP Production Requires Interaction with Adenosine A2b Receptor. *Nature* **2000**, *407*, 747−750.
(14) Peakman, M.-C.; Hill, S. J. Adenosine A_{2B}-receptor-mediated Cyclic AMP Accumulation in Primary Rat Astrocytes. *Br. J. Pharmacol.* **1994**, *111*, 191−198.
(15) Hua, X.; Kovarova, M.; Chason, K. D.; Nguyen, M.; Koller, B. H.; Tilley, S. L. Enhanced Mast Cell Activation in Mice Deficient in the A2b Adenosine Receptor. *J. Exp. Med.* **2007**, *204*, 117−128.
(16) Eckle, T.; Faigle, M.; Grenz, A.; Laucher, S.; Thompson, L. F.; Eltzschig, H. K. A2B Adenosine Receptor Dampens Hypoxia-Induced Vascular Leak. *Blood* **2008**, *111*, 2024−2035.
(17) Addi, A. B.; Lefort, A.; Hua, X.; Libert, F.; Communi, D.; Ledent, C.; Macours, P.; Tilley, S. L.; Boeynaems, J.-M.; Robaye, B. Modulation of Murine Dendritic Cell Function by Adenine Nucleotides and Adenosine: Involvement of the A2B Receptor. *Eur. J. Immunol.* **2008**, *38*, 1610−1620.
(18) Xaus, J.; Mirabet, M.; Lloberas, J.; Soler, C.; Lluis, C.; Franco, R.; Celada, A. IFN-γ Up-Regulates the A2B Adenosine Receptor Expression in Macrophages: A Mechanism of Macrophage Deactivation. *J. Immunol.* **1999**, *162*, 3607−3614.
(19) Kong, T.; Westerman, K. A.; Faigle, M.; Eltzschig, H. K.; Colgan, S. P. HIF-dependent Induction of Adenosine A2B Receptor in Hypoxia. *FASEB J.* **2006**, *20*, 2242−2250.
(20) Hart, M. L.; Jacobi, B.; Schittenhelm, J.; Henn, M.; Eltzschig, H. K. Cutting Edge: A2B Adenosine Receptor Signaling Provides Potent Protection during Intestinal Ischemia/Reperfusion Injury. *J. Immunol.* **2009**, *182*, 3965−3968.
(21) Haskó, G.; Csóka, B.; Németh, Z. H.; Vizi, E. S.; Pacher, P. A2B Adenosine Receptors in Immunity and Inflammation. *Trends Immunol.* **2009**, *30*, 263−270.
(22) Aherne, C. M.; Kewley, E. M.; Eltzschig, H. K. The Resurgence of A2B Adenosine Receptor Signaling. *Biochim. Biophys. Acta, Biomembr.* **2011**, *1808*, 1329−1339.
(23) Mittal, D.; Sinha, D.; Barkauskas, D.; Young, A.; Kalimutho, M.; Stannard, K.; Caramia, F.; Haibe-Kains, B.; Stagg, J.; Khanna, K. K.; Loi, S.; Smyth, M. J. Adenosine 2B Receptor Expression on Cancer Cells Promotes Metastasis. *Cancer Res.* **2016**, *76*, 4372−4382.
(24) Iannone, R.; Miele, L.; Maiolino, P.; Pinto, A.; Morello, S. Blockade of A2b Adenosine Receptor Reduces Tumor Growth and Immune Suppression Mediated by Myeloid-Derived Suppressor Cells in a Mouse Model of Melanoma. *Neoplasia* **2013**, *15*, 1400−1409.
(25) Gao, Z.-G.; Jacobson, K. A. A2B Adenosine Receptor and Cancer. *Int. J. Mol. Sci.* **2019**, *20*, 5139.
(26) Mousavi, S.; Panjehpour, M.; Izadpanahi, M. H.; Aghaei, M. Expression of Adenosine Receptor Subclasses in Malignant and Adjacent Normal Human Prostate Tissues. *Prostate* **2015**, *75*, 735−747.
(27) Novio, S.; Nuñez-Iglesias, M. J.; Freire-Garabal, M. Adenosine Signaling Pathways as Potential Therapeutic Targets in Prostate Cancer Disease. *Molecular Oncology: Underlying Mechanisms and Translational Advancements*; Springer International Publishing: Madrid, 2017; pp 93−107.
(28) Allard, D.; Turcotte, M.; Stagg, J. Targeting A2 Adenosine Receptors in Cancer. *Immunol. Cell Biol.* **2017**, *95*, 333−339.
(29) Sorrentino, C.; Morello, S. Role of Adenosine in Tumor Progression: Focus on A2B Receptor as Potential Therapeutic Target. *J. Cancer Metastasis Treat.* **2017**, *3*, 127.
(30) Sepúlveda, C.; Palomo, I.; Fuentes, E. Role of Adenosine A2b Receptor Overexpression in Tumor Progression. *Life Sci.* **2016**, *166*, 92−99.
(31) Morin, F.; Beauregard, J.-M.; Bergeron, M.; Nguile Makao, M.; Lacombe, L.; Fradet, V.; Fradet, Y.; Pouliot, F. Metabolic Imaging of Prostate Cancer Reveals Intrapatient Intermetastasis Response Heterogeneity to Systemic Therapy. *Eur. Urol. Focus* **2017**, *3*, 639−642.
(32) Wei, Q.; Costanzi, S.; Balasubramanian, R.; Gao, Z.-G.; Jacobson, K. A. A2B Adenosine Receptor Blockade Inhibits Growth of Prostate Cancer Cells. *Purinergic Signalling* **2013**, *9*, 271−280.
(33) Kaji, W.; Tanaka, S.; Tsukimoto, M.; Kojima, S. Adenosine A2B Receptor Antagonist PSB603 Suppresses Tumor Growth and Metastasis by Inhibiting Induction of Regulatory T Cells. *J. Toxicol. Sci.* **2014**, *39*, 191−198.
(34) Borrmann, T.; Hinz, S.; Bertarelli, D. C. G.; Li, W.; Florin, N. C.; Scheiff, A. B.; Müller, C. E. 1-Alkyl-8-(Piperazine-1-Sulfonyl)-Phenylxanthines: Development and Characterization of Adenosine A2B Receptor Antagonists and a New Radioligand with Subnanomolar Affinity and Subtype Specificity. *J. Med. Chem.* **2009**, *52*, 3994−4006.
(35) Jiang, J.; Seel, C. J.; Temirak, A.; Namasivayam, V.; Arridu, A.; Schabikowski, J.; Baqi, Y.; Hinz, S.; Hockemeyer, J.; Müller, C. E.

https://dx.doi.org/10.1021/acs.jmedchem.0c01431
J. Med. Chem. 2021, 64, 458−480

A2B Adenosine Receptor Antagonists with Picomolar Potency. *J. Med. Chem.* **2019**, *62*, 4032−4055.
(36) Hayallah, A. M.; Sandoval-Ramírez, J.; Reith, U.; Schobert, U.; Preiss, B.; Schumacher, B.; Daly, J. W.; Müller, C. E. 1,8-Disubstituted Xanthine Derivatives: Synthesis of Potent A2B-Selective Adenosine Receptor Antagonists. *J. Med. Chem.* **2002**, *45*, 1500−1510.
(37) Kim, Y.-C.; Ji, X.-d.; Melman, N.; Linden, J.; Jacobson, K. A. Anilide Derivatives of an 8-Phenylxanthine Carboxylic Congener Are Highly Potent and Selective Antagonists at Human A(2B) Adenosine Receptors. *J. Med. Chem.* **2000**, *43*, 1165−1172.
(38) Stewart, M.; Steinig, A. G.; Ma, C.; Song, J.-P.; McKibben, B.; Castelhano, A. L.; MacLennan, S. J. [3H]OSIP339391, a Selective, Novel, and High Affinity Antagonist Radioligand for Adenosine A2B Receptors. *Biochem. Pharmacol.* **2004**, *68*, 305−312.
(39) Taliani, S.; Pugliesi, I.; Barresi, E.; Simorini, F.; Salerno, S.; La Motta, C.; Marini, A. M.; Cosimelli, B.; Cosconati, S.; Di Maro, S.; Marinelli, L.; Daniele, S.; Trincavelli, M. L.; Greco, G.; Novellino, E.; Martini, C.; Da Settimo, F. 3-Aryl-[1,2,4]triazino[4,3-a]benzimidazol-4(10H)-one: A Novel Template for the Design of Highly Selective A2BAdenosine Receptor Antagonists. *J. Med. Chem.* **2012**, *55*, 1490−1499.
(40) Vidal, B.; Nueda, A.; Esteve, C.; Domenech, T.; Benito, S.; Reinoso, R. F.; Pont, M.; Calbet, M.; López, R.; Cadavid, M. I.; Loza, M. I.; Cárdenas, Á.; Godessart, N.; Beleta, J.; Warrellow, G.; Ryder, H. Discovery and Characterization of 4′-(2-Furyl)-N-Pyridin-3-yl-4,5′-Bipyrimidin-2′-Amine (LAS38096), a Potent, Selective, and Efficacious A2B Adenosine Receptor Antagonist. *J. Med. Chem.* **2007**, *50*, 2732−2736.
(41) El Maatougui, A.; Azuaje, J.; González-Gómez, M.; Miguez, G.; Crespo, A.; Carbajales, C.; Escalante, L.; García-Mera, X.; Gutiérrez-de-Terán, H.; Sotelo, E. Discovery of Potent and Highly Selective A2B Adenosine Receptor Antagonist Chemotypes. *J. Med. Chem.* **2016**, *59*, 1967−1983.
(42) Carbajales, C.; Azuaje, J.; Oliveira, A.; Loza, M. I.; Brea, J.; Cadavid, M. I.; Masaguer, C. F.; García-Mera, X.; Gutiérrez-de-Terán, H.; Sotelo, E. Enantiospecific Recognition at the A2B Adenosine Receptor by Alkyl 2-Cyanoimino-4-Substituted-6-Methyl-1,2,3,4-Tetrahydropyrimidine-5-Carboxylates. *J. Med. Chem.* **2017**, *60*, 3372−3382.
(43) Crespo, A.; El Maatougui, A.; Biagini, P.; Azuaje, J.; Coelho, A.; Brea, J.; Loza, M. I.; Cadavid, M. I.; García-Mera, X.; Gutiérrez-de-Terán, H.; Sotelo, E. Discovery of 3,4-Dihydropyrimidin-2(1H)-ones As a Novel Class of Potent and Selective A2B Adenosine Receptor Antagonists. *ACS Med. Chem. Lett.* **2013**, *4*, 1031−1036.
(44) Wilson, C. N.; Jamal, M. S. *Handbook of Experimental Pharmacology: Adenosine Receptors in Health and Disease*; Springer: Berlin, 2009.
(45) Baraldi, P. G.; Tabrizi, M. A.; Gessi, S.; Borea, P. A. Adenosine Receptor Antagonists: Translating Medicinal Chemistry and Pharmacology into Clinical Utility. *Chem. Rev.* **2008**, *108*, 238−263.
(46) Jacobson, K. A.; Tosh, D. K.; Jain, S.; Gao, Z.-G. Historical and Current Adenosine Receptor Agonists in Preclinical and Clinical Development. *Front. Cell. Neurosci.* **2019**, *13*, 124.
(47) Müller, C. E.; Baqi, Y.; Hinz, S.; Namasivayam, V. Medicinal Chemistry of A2B Adenosine Receptors. *Receptors* **2018**, *34*, 137−168.
(48) Kalla, R. V.; Zablocki, J. Progress in the Discovery of Selective, High Affinity A2B Adenosine Receptor Antagonists as Clinical Candidates. *Purinergic Signalling* **2009**, *5*, 21−29.
(49) Mallo-Abreu, A.; Majellaro, M.; Jespers, W.; Azuaje, J.; Caamaño, O.; García-Mera, X.; Brea, J. M.; Loza, M. I.; Gutiérrez-de-Terán, H.; Sotelo, E. Trifluorinated Pyrimidine-Based A2B Antagonists: Optimization and Evidence of Stereospecific Recognition. *J. Med. Chem.* **2019**, *62*, 9315−9330.
(50) Crespo, A.; El Maatougui, A.; Azuaje, J.; Escalante, L.; Majellaro, M.; Loza, M. I.; Brea, J.; Cadavid, M. I.; Gutiérrez-de-Terán, H.; Sotelo, E. Exploring the Influence of the Substituent at Position 4 in a Series of 3,4-Dihydropyrimidin-2(1H)-One A2B Adenosine Receptor Antagonists. *Chem. Heterocycl. Compd.* **2017**, *53*, 316−321.
(51) Kappe, C. O. Biologically Active Dihydropyrimidones of the Biginelli-Type - A Literature Survey. *Eur. J. Med. Chem.* **2000**, *35*, 1043−1052.
(52) Kappe, C. O. Recent Advances in the Biginelli Dihydropyrimidine Synthesis. New Tricks from an Old Dog. *Acc. Chem. Res.* **2000**, *33*, 879−888.
(53) Bose, D. S.; Fatima, L.; Mereyala, H. B. Green Chemistry Approaches to the Synthesis of 5-Alkoxycarbonyl-4-aryl-3,4- dihydropyrimidin-2(1H)-ones by a Three-Component Coupling of One-Pot Condensation Reaction: Comparison of Ethanol, Water, and Solvent-free Conditions. *J. Org. Chem.* **2003**, *68*, 587−590.
(54) Mobaraki, A.; Movassagh, B.; Karimi, B. Hydrophobicity-Enhanced Magnetic Solid Sulfonic Acid: A Simple Approach to Improve the Mass Transfer of Reaction Partners on the Surface of the Heterogeneous Catalyst in Water-Generating Reactions. *Appl. Catal., A* **2014**, *472*, 123−133.
(55) Ghasemi, Z.; Farshbaf Orafa, F.; Pirouzmand, M.; Zarrini, G.; Nikzad Kojanag, B.; Salehi, R. Zn^{2+}/MCM-41 Catalyzed Biginelli Reaction of Heteroaryl Aldehydes and Evaluation of the Antimicrobial Activity and Cytotoxicity of the Pyrimidone Products. *Tetrahedron Lett.* **2015**, *56*, 6393−6396.
(56) Agarwal, S.; Desai, R. Novel compounds for treatment of diabetes, obesity or related disorders. WO 2013102929 A1, 2013.
(57) Ali, F.; Khan, K. M.; Salar, U.; Iqbal, S.; Taha, M.; Ismail, N. H.; Perveen, S.; Wadood, A.; Ghufran, M.; Ali, B. Dihydropyrimidones: As novel class of β-glucuronidase inhibitors. *Bioorg. Med. Chem.* **2016**, *24*, 3624−3635.
(58) Zabihollahi, R.; Fassihi, A.; Aghasadeghi, M. R.; Memarian, H. R.; Soleimani, M.; Majidzadeh-A, K. Inhibitory Effect and Structure-Activity Relationship of Some Biginelli-Type Pyrimidines against HSV-1. *Med. Chem. Res.* **2013**, *22*, 1270−1276.
(59) Abdel-Fattah, A. A. Expedient Synthesis of Biginelli-Type Dihydropyrimidinones Using α-(Benzotriazolyl)alkyl Urea Derivatives. *Synthesis* **2003**, 2358−2362.
(60) Shamim, S.; Khan, K. M.; Salar, U.; Ali, F.; Lodhi, M. A.; Taha, M.; Khan, F. A.; Ashraf, S.; Ul-Haq, Z.; Ali, M.; Perveen, S. 5-Acetyl-6-Methyl-4-Aryl-3,4-Dihydropyrimidin-2(1H)-Ones: As Potent Urease Inhibitors; Synthesis, in Vitro Screening, and Molecular Modeling Study. *Bioorg. Chem.* **2018**, *76*, 37−52.
(61) Lacotte, P.; Buisson, D.-A.; Ambroise, Y. Synthesis, Evaluation and Absolute Configuration Assignment of Novel Dihydropyrimidin-2-Ones as Picomolar Sodium Iodide Symporter Inhibitors. *Eur. J. Med. Chem.* **2013**, *62*, 722−727.
(62) Uray, G.; Verdino, P.; Belaj, F.; Kappe, C. O.; Fabian, W. M. F. Absolute Configuration in 4-Alkyl- and 4-Aryl-3,4-Dihydro-2(1H)-Pyrimidones: A Combined Theoretical and Experimental Investigation. *J. Org. Chem.* **2001**, *66*, 6685−6694.
(63) Krenn, W.; Verdino, P.; Uray, G.; Faber, K.; Kappe, C. O. Determination of Absolute Configuration in 4-aryl-3,4-dihydro-2(1H)-pyrimidones by High Performance Liquid Chromatography and CD Spectroscopy. *Chirality* **1999**, *11*, 659−662.
(64) Crespo, A.; El Maatougui, A.; Biagini, P.; Azuaje, J.; Coelho, A.; Brea, J.; Loza, M. I.; Cadavid, M. I.; García-Mera, X.; Gutiérrez-de-Terán, H.; Sotelo, E. Discovery of 3,4-Dihydropyrimidin-2(1H)-ones As a Novel Class of Potent and Selective A2B Adenosine Receptor Antagonists. *ACS Med. Chem. Lett.* **2013**, *4*, 1031−1036.
(65) Liu, W.; Chun, E.; Thompson, A. A.; Chubukov, P.; Xu, F.; Katritch, V.; Han, G. W.; Roth, C. B.; Heitman, L. H.; Ijzerman, A. P.; Cherezov, V.; Stevens, R. C. Structural Basis for Allosteric Regulation of GPCRS by Sodium Ions. *Science* **2012**, *337*, 232−236.
(66) Jaakola, V.-P.; Griffith, M. T.; Hanson, M. A.; Cherezov, V.; Chien, E. Y. T.; Lane, J. R.; Ijzerman, A. P.; Stevens, R. C. The 2.6 Å Crystal Structure of a Human A2A Adenosine Receptor Bound to an Antagonist. *Science* **2008**, *322*, 1211−1217.
(67) Bortolato, A.; Tehan, B. G.; Bodnarchuk, M. S.; Essex, J. W.; Mason, J. S. Water Network Perturbation in Ligand Binding:

Adenosine A2A Antagonists as a Case Study. *J. Chem. Inf. Model.* **2013**, *53*, 1700−1713.
(68) Nayadu, S.; Behera, D.; Sharma, M.; Kaur, G.; Gudi, G. Fluorescent Probe Based CYP Inhibition Assay: A High Throughput Tool for Early Drug Discovery Screening. *Int. J. Pharm. Sci.* **2013**, *5*, 303−307.
(69) McDonnell, A. M.; Dang, C. H. Basic Review of the Cytochrome P450 System. *J. Adv. Pract. Oncol.* **2013**, *4*, 263−268.
(70) Guengerich, F. P.; Waterman, M. R.; Egli, M. Recent Structural Insights into Cytochrome P450 Function. *Trends Pharmacol. Sci.* **2016**, *37*, 625−640.
(71) Guengerich, F. P. Cytochrome P450 and Chemical Toxicology. *Chem. Res. Toxicol.* **2008**, *21*, 70−83.
(72) Virtanen, S. S.; Kukkonen-Macchi, A.; Vainio, M.; Elima, K.; Härkönen, P. L.; Jalkanen, S.; Yegutkin, G. G. Adenosine Inhibits Tumor Cell Invasion via Receptor-Independent Mechanisms. *Mol. Cancer Res.* **2014**, *12*, 1863−1874.
(73) Vijayan, D.; Young, A.; Teng, M. W. L.; Smyth, M. J. Targeting Immunosuppressive Adenosine in Cancer. *Nat. Rev. Cancer* **2017**, *17*, 709−724.
(74) Chen, S.; Akdemir, I.; Fan, J.; Linden, J.; Zhang, B.; Cekic, C. The Expression of Adenosine A2B Receptor on Antigen-Presenting Cells Suppresses CD8+ T-cell Responses and Promotes Tumor Growth. *Cancer Immunol. Res.* **2020**, *8*, 1064−1074.
(75) Bahreyni, A.; Samani, S. S.; Rahmani, F.; Behnam-Rassouli, R.; Khazaei, M.; Ryzhikov, M.; Parizadeh, M. R.; Avan, A.; Hassanian, S. M. Role of Adenosine Signaling in the Pathogenesis of Breast Cancer. *J. Cell. Physiol.* **2018**, *233*, 1836−1843.
(76) Dhar, S.; Gu, F. X.; Langer, R.; Farokhzad, O. C.; Lippard, S. J. Targeted Delivery of Cisplatin to Prostate Cancer Cells by Aptamer Functionalized Pt(IV) Prodrug-PLGA−PEG Nanoparticles. *Proc. Natl. Acad. Sci. U.S.A.* **2008**, *105*, 17356−17361.
(77) Núñez-Iglesias, M. J.; Novio, S.; García-Santiago, C.; Cartea, M. E.; Soengas, P.; Velasco, P.; Freire-Garabal, M. Effects of 3-Butenyl Isothiocyanate on Phenotypically Different Prostate Cancer Cells. *Int. J. Oncol.* **2018**, *53*, 2213−2223.
(78) Mao, L.; Yang, C.; Wang, J.; Li, W.; Wen, R.; Chen, J.; Zheng, J. SATB1 Is Overexpressed in Metastatic Prostate Cancer and Promotes Prostate Cancer Cell Growth and Invasion. *J. Transl. Med.* **2013**, *11*, 111.
(79) Hejchman, E.; Taciak, P.; Kowalski, S.; Maciejewska, D.; Czajkowska, A.; Borowska, J.; Śladowski, D.; Młynarczuk-Biały, I. Synthesis and Anticancer Activity of 7-Hydroxycoumarinyl Gallates. *Pharmacol. Rep.* **2015**, *67*, 236−244.
(80) Härmä, V.; Haavikko, R.; Virtanen, J.; Ahonen, I.; Schukov, H.-P.; Alakurtti, S.; Purev, E.; Rischer, H.; Yli-Kauhaluoma, J.; Moreira, V. M.; Nees, M.; Oksman-Caldentey, K.-M. Optimization of Invasion-Specific Effects of Betulin Derivatives on Prostate Cancer Cells through Lead Development. *PLoS One* **2015**, *10* (). DOI: 10.1371/journal.pone.0126111.
(81) Bai, S.; Herrera-Abreu, M.; Rohn, J. L.; Racine, V.; Tajadura, V.; Suryavanshi, N.; Bechtel, S.; Wiemann, S.; Baum, B.; Ridley, A. J. Identification and Characterization of a Set of Conserved and New Regulators of Cytoskeletal Organization, Cell Morphology and Migration. *BMC Biol.* **2011**, *9*, 54.
(82) Jackson, S. J. T.; Singletary, K. W.; Venema, R. C. Sulforaphane Suppresses Angiogenesis and Disrupts Endothelial Mitotic Progression and Microtubule Polymerization. *Vasc. Pharmacol.* **2007**, *46*, 77−84.
(83) *Schrödinger*; Schrödinger LLC: New York, 2009.
(84) Rodríguez, D.; Piñeiro, Á.; Gutiérrez-De-Terán, H. Molecular Dynamics Simulations Reveal Insights into Key Structural Elements of Adenosine Receptors. *Biochemistry* **2011**, *50*, 4194−4208.
(85) Šali, A.; Blundell, T. L. Comparative Protein Modelling by Satisfaction of Spatial Restraints. *J. Mol. Biol.* **1993**, *234*, 779−815.
(86) Gutiérrez-de-Terán, H.; Bello, X.; Rodríguez, D. Characterization of the Dynamic Events of GPCRs by Automated Computational Simulations. *Biochem. Soc. Trans.* **2013**, *41*, 205−212.
(87) Hess, B.; Kutzner, C.; Van Der Spoel, D.; Lindahl, E. GROMACS 4: Algorithms for Highly Efficient, Load-Balanced, and Scalable Molecular Simulation. *J. Chem. Theory Comput.* **2008**, *4*, 435−447.
(88) Kaminski, G. A.; Friesner, R. A.; Tirado-Rives, J.; Jorgensen, W. L. Evaluation and Reparametrization of the OPLS-AA Force Field for Proteins via Comparison with Accurate Quantum Chemical Calculations on Peptides. *J. Phys. Chem. B* **2001**, *105*, 6474−6487.
(89) Berger, O.; Edholm, O.; Jähnig, F. Molecular Dynamics Simulations of a Fluid Bilayer of Dipalmitoylphosphatidylcholine at Full Hydration, Constant Pressure, and Constant Temperature. *Biophys. J.* **1997**, *72*, 2002−2013.
(90) Marelius, J.; Kolmodin, K.; Feierberg, I.; Åqvist, J. Q: A Molecular Dynamics Program for Free Energy Calculations and Empirical Valence Bond Simulations in Biomolecular Systems. *J. Mol. Graphics Modell.* **1998**, *16*, 213−225.
(91) Jespers, W.; Esguerra, M.; Åqvist, J.; Gutiérrez-de-Terán, H. Qligfep: An Automated Workflow for Small Molecule Free Energy Calculations in Q. *J. Cheminf.* **2019**, *11*, 1−16.
(92) King, G.; Warshel, A. A Surface Constrained All-Atom Solvent Model for Effective Simulations of Polar Solutions. *J. Chem. Phys.* **1989**, *91*, 3647−3661.
(93) Lee, F. S.; Warshel, A. A Local Reaction Field Method for Fast Evaluation of Long-Range Electrostatic Interactions in Molecular Simulations. *J. Chem. Phys.* **1992**, *97*, 3100−3107.
(94) Ryckaert, J.-P.; Ciccotti, G.; Berendsen, H. J. C. Numerical Integration of the Cartesian Equations of Motion of a System with Constraints: Molecular Dynamics of n-Alkanes. *J. Comput. Phys.* **1977**, *23*, 327−341.
(95) Robertson, M. J.; Tirado-Rives, J.; Jorgensen, W. L. Improved Peptide and Protein Torsional Energetics with the OPLS-AA Force Field. *J. Chem. Theory Comput.* **2015**, *11*, 3499−3509.
(96) Bennett, C. H. Efficient Estimation of Free Energy Differences from Monte Carlo Data. *J. Comput. Phys.* **1976**, *22*, 245−268.